JOHANNES GUTENBERG
UNIVERSITÄT MAINZ

Dissertation zur Erlangung des Grades
"Doktor der Naturwissenschaften"
im Promotionsfach Chemie

Stabilizing Molecular Self-Assemblies via On-Surface Reactions

Robert Lindner

geboren in Leonberg

Mainz, den 27. Februar 2015

This thesis was supervised by [redacted] and was carried out at the Johannes Gutenberg-Universität Mainz from March 2012 to March 2015.

D77 (Dissertation Johannes Gutenberg-Universität Mainz)

Dean of the Faculty	[redacted]
1st report	[redacted] Johannes Gutenberg-Universität Mainz
2nd report	[redacted] Johannes Gutenberg-Universität Mainz
Submitted:	27 February 2015
Oral examination:	22 April 2015

Abstract

Future technologies such as molecular electronics require the creation of functional structures directly on solid surfaces. For this task, molecular self-assembly has been identified as a most-promising bottom-up approach. The challenge, herein, is to find a fine balance between intramolecular interaction and the interaction between substrate and molecules. However, since molecular self-assembly relies solely on reversible interactions, the structures formed are inherently unstable. Thus, the creation of covalent bonds via on-surface reactions is of utmost importance in the development of molecular devices.

Therefore, in this thesis, strategies needed for the precise modification of self-assembled structures and novel concepts for on-surface reactions are presented. Using state-of-the-art non-contact atomic force microscopy in ultra-high-vacuum, which allows for imaging individual molecules on bulk insulators, the decisive influence of anchor moieties on the molecular self-assembly was shown. Furthermore, the stability of self-assembled structures was greatly enhanced by controlling on-surface reactions and enhancing molecule-substrate interactions.

The decisive influence of electrostatic anchors is demonstrated by the comparison of an aromatic molecule and its fourfold chlorinated derivative. For these molecules, strikingly divergent self-assembly behaviour was observed. It is shown that the ability to self-assemble into stable molecular islands, is driven by the substituents and the dimensions of the molecules.

Within this work the photochemical reaction of organic molecules on a bulk insulator is demonstrated for the first time. The reaction is forced into a specific direction by the dimensions of the underlying substrate, which was corroborated by a thorough statistical analysis.

Furthermore, a general concept for the enhancement of self-assembled structures, based on the controlled transfer of electrons, is presented. With an increasing amount of charge-donating atoms, the thermal stability of molecular islands is shown to be significantly enhanced. Additionally, the desorption behaviour of the islands is distinctively changed by the doping process.

In conclusion, this thesis evaluates and successfully applies strategies designed to steer the process of molecular self-assembly and the concepts needed to stabilize and modify self-assembled structures.

Abstract (german)

Für die Realisierung zukünftiger Technologien, wie z.B. molekulare Elektronik, werden Strategien benötigt, um funktionale Strukturen direkt auf Oberflächen zu erzeugen. Für die Bewältigung dieser Aufgabe ist die molekulare Selbstanordnung ein äußerst vielversprechender Bottom-up-Ansatz. Hierbei ist eine der größten Herausforderungen das Zusammenspiel aus intramolekularer Wechselwirkung und der Wechselwirkung zwischen Substrat und Molekülen in ein Gleichgewicht zu bringen. Da jedoch die wirkenden Kräfte der molekularen Selbstanordnung ausschließlich reversibler Natur sind, ist eine langfristige Stabilität fragwürdig. Somit ist die kovalente Verknüpfung der gebildeten Strukturen durch Reaktionen direkt auf der Oberfläche unerlässlich, um die Stabilität der Strukturen weiter zu erhöhen.

Hierzu stellt die vorliegende Arbeit eine ausführliche Studie zu molekularer Selbstanordnung und der zielgerichteten Modifikation ebensolcher Strukturen dar. Durch den Einsatz von hochauflösender Rasterkraftmikroskopie im Ultrahochvakuum, welche es erlaubt einzelne Moleküle auf Nichtleitern abzubilden, wurde der maßgebliche Einfluss von Ankerfunktionalitäten auf den Prozess der molekularen Selbstanordnung gezeigt. Des Weiteren konnte die Stabilität der selbst angeordneten Strukturen durch neue Oberflächenreaktionskonzepte entschieden verbessert werden.

Der Einfluss von Ankerfunktionen, die elektrostatische Wechselwirkung zwischen Molekül und Substrat vermitteln, auf den Strukturbildungsprozess der molekularen Selbstanordnung wird eingehend durch den Vergleich eines aromatischen Moleküls und seines vierfach chlorierten Derivates gezeigt. Für diese beiden Moleküle wurde ein deutlich unterschiedliches Verhalten der Selbstanordnung beobachtet. Es wird gezeigt, dass die Fähigkeit zur Bildung selbst angeordneter, stabiler Inseln entscheidend durch die Substituenten und die Abmessungen des Moleküls beeinflusst wird.

Auch wird in dieser Arbeit die erste photochemische Reaktion organischer Moleküle auf einem Isolator gezeigt. Qualitative und quantitative Ergebnisse liefern ein detailliertes Bild darüber, wie die Abmessungen des Substratgitters die Richtung der Reaktion gezielt beeinflussen.

Des Weiteren wird ein allgemeines Konzept zur selektiven Stabilisierung selbstangeordneter Molekülstrukturen durch den kontrollierten Transfer von Elektronen präsentiert. Durch die gezielte Steuerung der Menge an Dotierungsatomen wird die Desorptionstemperatur der molekularen Inseln signifikant erhöht und das Desorptionsverhalten der Inseln entschieden verändert.

Diese Arbeit präsentiert somit erfolgreich durchgeführte Strategien um den Prozess der molekularen Selbstanordnung zu steuern, sowie entscheidende Mechanismen um die Stabilisierung und Modifizierung von selbst angeordneten Strukturen zu gewährleisten.

Kein überflüssiges Wort zuviel.

— **Angelika Kühnle**

Für Kristina

Contents

1 Introduction

In the bygone century semiconductor technology has triggered an enormous field of research. Starting from devices on the scale of several centimeters down to modern transistors being in the 10-20 nm regime, the number of atoms needed to store one bit of information has reduced from 10^{19} atoms in 1960 to about 10^{3} atoms in 2010.[1] For the creation of these structures two different approaches can be thought of, namely *top-down* and *bottom-up*. Top-down approaches start with a large amount of material. Step-by-step, material is removed, until only the desired shape is left. Typical examples for top-down processes are the classical methods to create semiconductor devices, e.g., lithography and etching. The bottom-up approach starts from single building blocks, which are smaller than the resulting structure. By combining the building blocks, the desired structure is obtained.

The classical top-down methods are expected to reach their miniaturization limits until 2020.[2] Hence, exploring bottom-up methods is mandatory for the continuous miniaturization of structures in electronic devices. Recent advances have proven the ability to manipulate individual atoms and molecules. While this is a very impressive achievement, it is also very time consuming. In particular, atom-by-atom manipulation is unlikely to provide the efficiency needed for mass production. This is given by the *serial* nature of this approach, only allowing for one manipulation step at a time.

In order to follow a *parallel* approach, molecular self-assembly is most promising since it allows for the creation of structures at the atomic level.[3] Self-assembly of molecules relies on two interactions, namely the intermolecular and the molecule-surface interactions. By deliberately tuning the involved interactions, the resulting structures can be controlled, explaining the great success of molecular self-assembly for functional structure formation. However, since molecular self-assembly solely relies on reversible interactions, the resulting structures are inherently instable. Thus, strategies are required to stabilize these structures. Here, on-surface synthesis has proven to be a most promising approach.[4] Furthermore, on-surface synthesis is able to provide fully conjugated networks. These are desirable because of their electron transport properties, especially when envisioning future technologies like molecular electronics. Another highly exciting aspect of on-surface synthesis is the chance to discover new reaction pathways due to the two-dimensional confinement of the reaction educts.

In this thesis, the aforementioned concepts of molecular self-assembly and on-surface thesis will be used for the creation of molecular structures on an insulating substrate, namely the calcite (10.4) cleavage plane. The technique used to unravel the processes at the molecular scale is state-of-the-art non-contact atomic force microscopy operated under ultra-high vacuum (UHV) conditions. This technique allows for imaging insulating substrates and the molecules adsorbed onto the surface in real space with atomic precision. Therefore, in chapter 2 the underlying principles of this measurement technique will be introduced.

The insulator of choice in this thesis is calcite, since this material has proven to be a versatile substrate for molecular self-assembly.[5] Hence, in chapter 3, the properties of calcite will be concisely discussed. A more detailed focus is lying on the (10.4) cleavage plane, since it is the underlying substrate for all experiments discussed herein. In the successive chapter 4, I will give a comprehensive overview over the highly active field of on-surface synthesis. Starting from the first steps on metal surfaces at the beginning of this century, I will furthermore discuss the very recent investigations of thermally activated on-surface synthesis on insulators.

In chapter 6, I will present my results on how electrostatic anchors built into perylene derivatives influence and stabilize the structures formed in the reversible process of self-assembly. While ordered structures can be achieved, these molecular arrangements will always lack the thermal and chemical stability that is offered by covalently bonded networks. Consequently, chapter 7 will present a photochemical approach for the creation of covalent bonds. I will show that the choice of substrate is crucial for controlling the direction of the reaction. Furthermore, I will present a statistical analysis, quantifying the directionality of the reaction. Chapter 8 will describe how atomic doping directly influences the properties of self-assembled structures. It will be demonstrated that the controlled dosing of a reaction partner has the ability to increase the thermal stability of molecular islands and that the disintegration procedure during desorption is significantly altered.

Thus, the results of this thesis present an important insight into the nature of molecular self-assembly and the strategies needed for the stabilization and modification of self-assembled structures. This thesis will, therefore, be beneficial for the further development of tailor-made molecular structures, especially in the context of creating future technologies like molecular electronics via the bottom-up approach.

2 Atomic Force Microscopy

The most widely used chemical analysis methods, e.g. infra-red spectroscopy, x-ray diffraction or nuclear magnetic resonance spectroscopy, are highly valuable tools for chemists and physicists to unravel the properties and the behaviour of all kinds of compounds and materials. However, all these techniques reveal information in a way that most of the time is not straightforward in analysis. Furthermore, these techniques usually do not reveal information on a local scale. In order to obtain such local information, at best at the single-molecule level, the usage of microscopy techniques comes to mind. However, due to the diffraction limit of classic optical microscopes,[6] which is directly connected to the used wavelength, resolving molecular and atomic structures is quite challenging.[7]

The first steps towards the broad field of scanning probe microscopy (SPM) were accomplished by R. Young, J. Ward and F. Scire in 1972.[8] Their so-called topografiner already included nearly all features of a modern scanning tunnelling microscope (STM). Operating under high-vacuum conditions, they used the field-emission current to record the topography of a diffraction grating with a lateral resolution of 400 nm. Furthermore, they could show a distance dependant metal-vacuum-metal tunnelling current.
The first real surface study with an STM was conducted by Binnig, Rohrer and Gerber in 1981.[9] Due to the exponential distance dependence of the tunnelling current, they could already resolve monatomic steps on a $CaIrSn_4$ (110) surface with a lateral resolution of 1 nm. Only five years after this invention, Binnig, Quate and Gerber presented the atomic force microscope (AFM).[10]

2.1 General Setup

All SPM methods are based on the same main principle. A tip is positioned close to a surface and scanned in a line-by-line fashion over the surface. This movement is conducted by an XYZ-Scanner, which typically consists of a piezo tube. Here, an external voltage is applied to the tube and translated into a deformation of the piezo crystal. This deformation causes a displacement of the tip and allows for sub-nanometer movements.[10] While scanning, the interaction between tip and sample is recorded, and, depending on the scanning mode, fed into a feedback loop

which tries to keep the tip sample interaction constant at a pre-set value, i.e. by controlling the tip-sample distance via the scanning piezo.

Please note that the measured interaction can be of manifold origin. Typical measurement signals are for example tunnelling current, chemical bonding forces, Pauli repulsion, or magnetic forces. This large variety of measurable quantities makes the field of SPM a highly versatile method for the investigation of surfaces in real-space.

The AFM employs a micro-machined cantilever (see Fig. 2.1 A) which is usually made out of silicon or silicon nitride.[11] At the very end of the cantilever the conical tip is positioned, which, in the ideal case, reduces to a single atom at the tip apex (see Fig. 2.1 B). The most widely used way to detect a change in interaction between tip and sample uses a laser beam which is reflected at the back side of the cantilever and is detected at a 4-quadrant position sensitive diode (PSD) (see Fig. 2.1 C). When the tip-sample interaction changes the bending of the cantilever, the incident angle of the laser beam on the cantilever backside changes accordingly. Thus, the reflected laser beam illuminates a different position on the PSD, resulting in a change in current, proportional to the cantilever displacement. With the AFM, the effect of the force between tip and sample is measured.

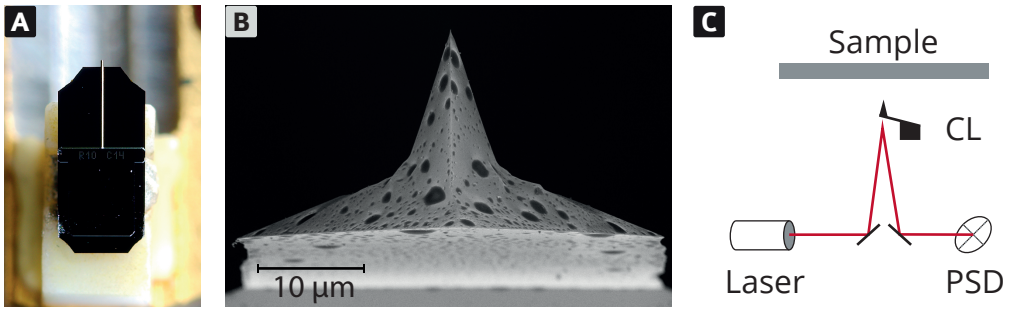

Fig. 2.1.: *(a)* Close-up of a micro-machined cantilever chip; *(b)* SEM image of a cantilever (image courtesy of Jannis Lübbe); *(c)* Schematic setup of a beam-deflection AFM (CL = Cantilever, PSD = position sensitive diode).

2.2 Operating Modes

Like any SPM method, the AFM can be operated in various modes. All of these scanning modes can be performed with or without the use of a feedback loop. When no feedback loop is used, the piezo displacement does not change over time, thus, the absolute height of the cantilever does not change. Hence, it is referred to as *constant height mode*. When the feedback loop is activated, the mode is called *constant force/amplitude/detuning*, where the exact name depends on the measured quantity.

The simplest mode is the *static* or *contact mode* (see Fig. 2.2 A). By constantly pressing the cantilever onto the surface, the cantilever is bend due to Pauli repulsion. When the sample topology changes, the bending of the cantilever is also changed. This bending is detected by a PSD and, depending on the scanning mode, fed into a feedback loop, which tries to keep the force acting on the cantilever at a constant value, by varying the distance between tip and sample. As easily evident, the simplicity is paid for by accepting severe drawbacks. Due to the contact between tip and sample, the tip loses its sharpness rather quickly. This results in a diminished resolution, because the contact area is several nm^2 large. At best, lattice resolution can be achieved, where the crystal lattice of the tip is scanned over the crystal lattice of the sample, thus, making the detection of atomic defects impossible. Additionally, shearing forces acting between the cantilever and the sample can easily result in the destruction of soft samples.

In the intermittent contact mode (see Fig. 2.2 B), the cantilever is driven near its resonance frequency and periodically taps onto the surface. By a change in tip-sample interaction, the oscillation amplitude changes. Again, this change in measurement signal can be kept constant by a feedback loop, and, thus, the topology of the sample is mapped. Yet, the resolution limit is still comparable to the contact mode, since a rather large area is in contact with the sample. Shearing forces are, however, avoided. Hence, soft samples can be investigated without destroying their surface.

The highest resolution is achieved with the non-contact mode. Here, either the

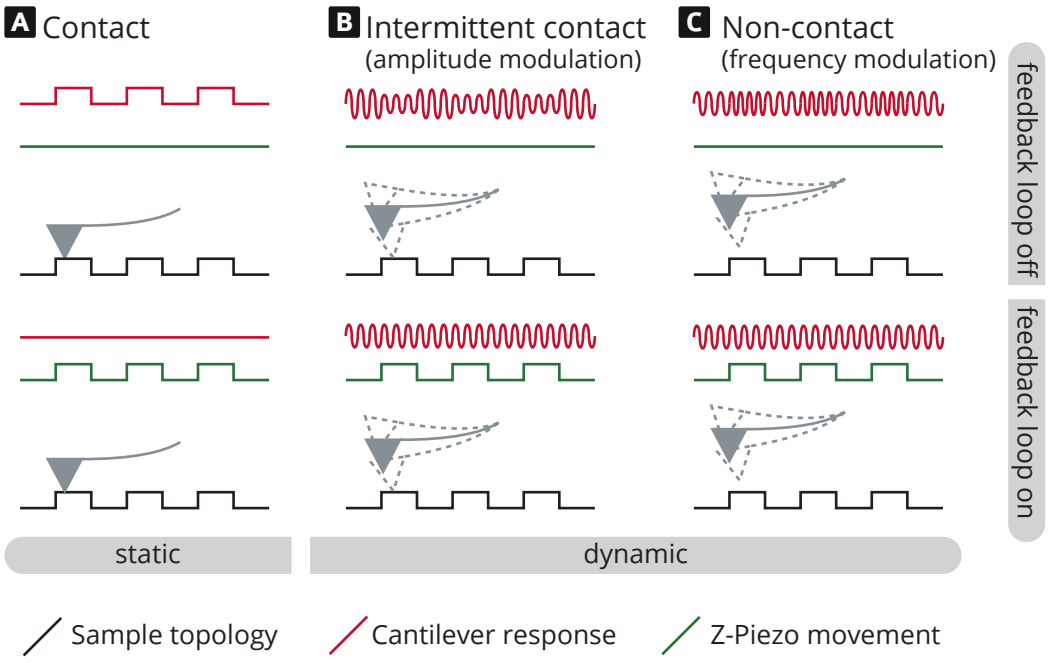

Fig. 2.2.: Schematic view over the most common scanning modes and the resulting signals.

amplitude or the frequency (see Fig. 2.2 C) of the oscillating cantilever can be modulated. However, when measuring in UHV amplitude-modulation-atomic force

microscope has the tremendous disadvantage that the response time τ_{AM} of the cantilever to changes in the tip-sample force is directly proportional to the quality factor Q of the cantilever, as evident from the relation[12]

$$\tau_{AM} \approx \frac{2Q}{f_0}. \tag{2.1}$$

High Q factors, which are typical for UHV,[a] prolong the response time of the system and demand low scanning rates. Thus, AM-AFM is not feasible under UHV conditions, but is a technique used in ambient conditions, where the Q factor is much smaller.

Instead frequency-modulation (FM) AFM is used under UHV conditions.

2.3 FM-AFM

In 1991, Albrecht and co-workers managed to combine high scan speed and low noise, due to high Q factors, by introducing the FM mode.[13] Here the cantilever is oscillated at its eigenfrequency f, while keeping the amplitude constant (see Fig. 2.2 (C)). Tip-sample interactions shift the eigenfrequency f_0 of the unperturbed cantilever by Δf, where

$$\Delta f = f - f_0. \tag{2.2}$$

If we assume the cantilever to be a harmonic oscillator, we can express the eigenfrequency as

$$f_0 = \frac{1}{2\pi}\sqrt{\frac{k}{m*}} \tag{2.3}$$

with m^* and k being the effective mass and the spring constant of the cantilever, respectively.

By approaching the tip to the immediate vicinity of the surface, the oscillating tip is affected by the forces arising from the tip-sample interaction (see Sec. 2.4). For small variations in the tip-sample distance the force gradient k_{ts} can be expected to be constant, and, thus, Eqn. 2.3 can be complemented by $k_{ts} = \partial F_{ts}/\partial z$:[12]

$$f = \frac{1}{2\pi}\sqrt{\frac{k - \frac{\partial F_{ts}}{\partial z}}{m^*}}. \tag{2.4}$$

[a] Typical values for Q in UHV are $10^4 < Q < 10^5$, due to the reduced air damping

In order to mathematically connect Δf and k_{ts}, the Eqns. 2.3 and 2.4 can be inserted into Eqn. 2.2. For the case $k_{ts} << k$, the resulting expression can be simplified via a Taylor series and, thus, the frequency shift[12]

$$\Delta f = -\frac{f_0}{2k}\frac{\partial F_{ts}}{\partial z} = -\frac{f_0}{2k} \cdot k_{ts}. \tag{2.5}$$

This equation is only correct if the force gradient is constant during one period of oscillation, which is only the case for small amplitudes.
Albeit these drawbacks, FM-afm is a most valuable technique since frequencies can be measured with utmost precision, achieving uncertainties as low as $1.4 \cdot 10^{-17}$ Hz, even when measuring in the THz regime.[14] Therefore, the detuning of the oscillating cantilever can be used as a direct measurement signal, viz. the *constant-height mode*, or processed by a feedback loop, yielding a topography of the sample, viz. the *constant-detuning mode*. In all cases a phase-locked loop (PLL) is used to keep the phase between the cantilever oscillation and a reference oscillation constant.[15]

2.4 Imaging Principle

The imaging signal in AFM arises from the potential energy V_{ts} between tip and sample. This potential gives rise to a force F_{ts} between tip and sample in z-direction

$$F_{ts} = -\frac{\partial V_{ts}}{\partial z}. \tag{2.6}$$

When trying to model this potential qualitatively, the semi-empirical Lennard-Jones-Potential is often considered,[16] which has the general form

$$V_{Lennard-Jones} = -V_0 \cdot (2 \cdot \frac{z_0}{z}^6 - \frac{z_0}{z}^1 2). \tag{2.7}$$

The attractive interaction between tip and sample is described by the first part in equation 2.7. This part arises from van-der-Waals forces. The second part describes the Pauli repulsion. However, it has to be noted that the Lennard-Jones-Potential only describes the interaction between uncharged and chemically non-bonding particles.

The Lennard-Jones potential, its contributing terms and the resulting force are visualized in Fig. 2.3. As can be clearly seen, the interplay between attractive and repulsive forces result in a potential minimum at the equilibrium distance z_0, with a value of $-V_0$. In this point the corresponding force $F_{ts} = 0$.

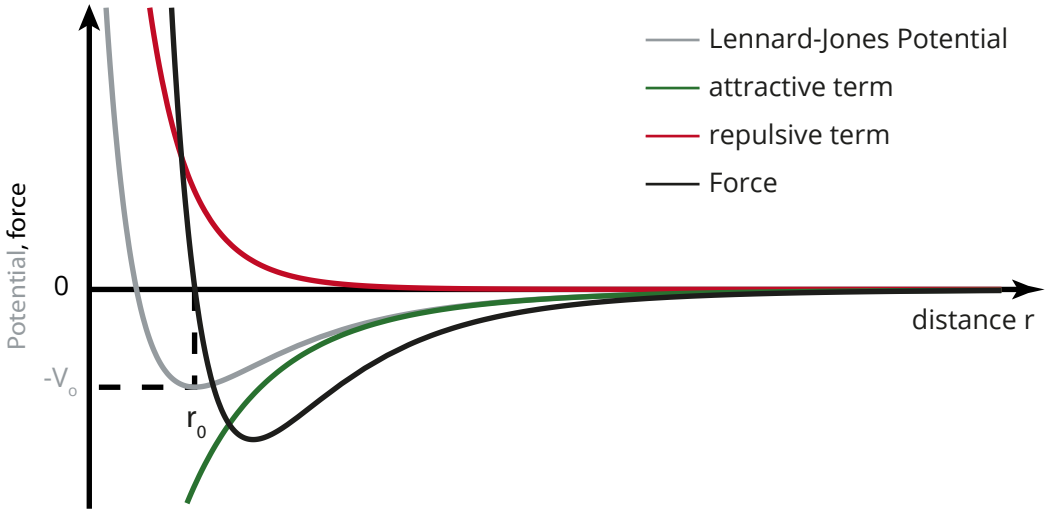

Fig. 2.3.: Plot of the Lennard-Jones potential and its corresponding attractive and repulsive terms.

To further characterize the interaction, the individual contributions will be discussed in the following section.

2.4.1 Long-range forces

The long-range contributions to the total force F_{ts} mainly consist of electrostatic forces and Van-der-Waals forces. Due to their long range, macroscopic areas of the tip and the sample contribute to this force and, thus, atomic resolution with these contributions is impossible. Consequently, these contributions should be compensated for, e.g. by applying an external bias voltage to counterbalance electrostatic forces.

Electrostatic forces

The electrostatic interaction between atoms is be described by the Coulomb interaction. By placing two point charges 1 and 2 with charge q_1 and q_2 at a distance z, the resulting force $F_C(z)$ is

$$F_C(z) = \frac{1}{4\pi\epsilon_0}\frac{q_1 \cdot q_2}{z^2} \tag{2.8}$$

with ϵ_0 being the dielectric constant.

Van-der-Waals forces

The long-range van-der-Waals (vdW) forces arise from the interaction of dipoles and are typically separated into three different contributions, base on the combination of permanent and induced dipoles.

Keesom interaction occurs when two permanent dipoles interact with each other. When one permanent dipole induces a temporary dipole in another polarizable particle, the resulting force is described by *Debye interaction*.
Given the fact that electron clouds fluctuate over time, a temporary dipole can arise, which induces another temporary dipole in a neighboring particle and vice versa. This effect is described by the *London dispersion force*.

2.4.2 Short-range Forces

Atomic imaging contrast in AFM relies on short-range interaction between tip and sample. These contribution to F_{ts} mainly consist of Pauli repulsion and chemical bonding.

Pauli repulsion
Pauli repulsion is a quantum mechanical effect between particles. The Pauli exclusion principle states that two fermions occupying the same space (e.g. electrons) cannot be identical in all quantum numbers. When tip and sample are approached, at some point their orbitals will need to overlap. When these orbitals are fully populated, the electrons therein will not differ in their quantum numbers. Thus, the overlap of two fully occupied orbitals is impossible and, thus, gives rise to a repulsive interaction since the electrons are forced to occupy states with higher energy.

Chemical bonding
The exchange interaction between orbitals is an attractive force. Covalent bonds can be formed between tip and sample, if the orbitals are not fully occupied. Due to the scanning movement, however, these bonds are broken again immediately.

2.5 Imaging Artifacts

Artifacts in SPM images are based on the fact, that the measured signal is always a convolution between the properties of tip and sample. For the case of STM the influence of the tip shape on the distortion of the images is not that crucial, since the measurement signal, i.e. the tunneling current, has an exponential decay with respect to the distance. In AFM, however, this distance dependence is reduced to z^6 or even a lower power, as discussed above in sec. 2.4. Hence, the microscopic tip geometry is of much greater importance for the quality of the obtained images.

The most prominent cases are depicted in Fig. 2.4, based on the assumption of a conical tip. When the opening angle α of the tip is smaller than the opening angle β of the feature (Fig. 2.4 A), the scanned feature will be imaged correctly. If, on the other hand, the opening angle α of the tip is larger than the opening angle β of

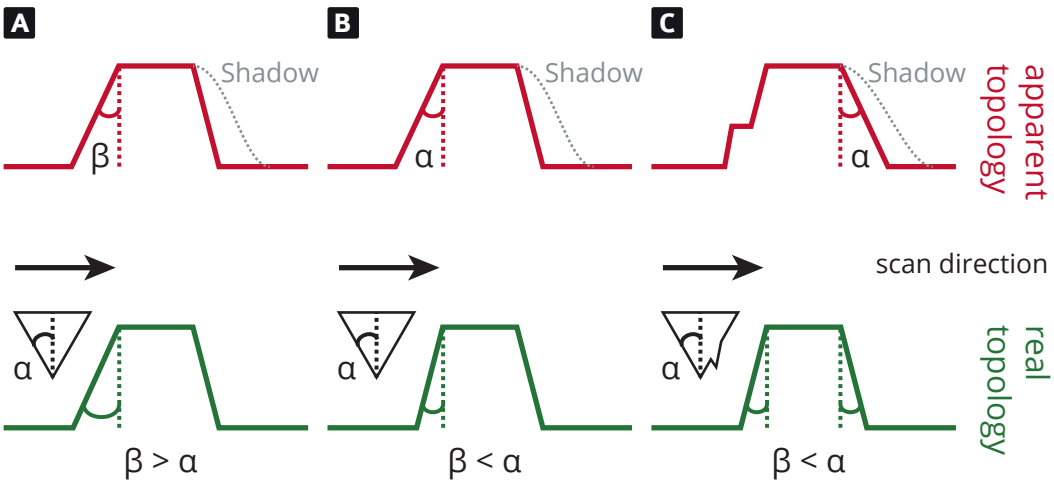

Fig. 2.4.: Imaging artifacts for several cases: (A) In the ideal case, the opening angle β of the sample is larger than the opening angle α of the tip; (B) If $\beta \leq \alpha$, the apparent opening angle of the feature is α; (C) A double tip produces apparent kink sites on the side of the feature facing the fast scan direction.

the feature, then the apparent angle of the feature will be α (Fig. 2.4 B). These two cases are only true given that a perfectly symmetrical tip is used, which is not a realistic assumption. In reality the tip exhibits asymmetries, as depicted exemplarily in Fig. 2.4 C. The double tip feature leads to an apparent kink site on the side of the feature. Furthermore, if the two tips are separated even more, small features can be imaged twice in one image. However, it has to be noted that the previously discussed examples are only exactly true for an infinitely fast feedback loop. If the feedback loop behaves realistically, i.e. with a finite response time, a shadow at the backside of the feature, with respect to the scan direction, can be observed (see the gray lines in Fig. 2.4).

2.6 Basic Setup

The general setup of a beam-deflection non-contact atomic force microscope (NC-AFM) is depicted in Fig. 2.5. The excitation piezo is driven by a voltage supplied by the amplitude feedback loop (A-FB). This results in an oscillation of the cantilever. Consequently. a laser beam, which is focused on the backside of the cantilever, gets deflected and, thus, changes its position on the 4-quadrant PSD. Since each quadrant converts incident light into a voltage proportional to the light intensity, simple arithmetics of these signals yield a sinusoidal voltage proportional to the current force, namely F_N. This signal is then fed back into the PLL and the A-FB. The PLL then determines the current frequency f of the oscillating cantilever and gives the frequency shift Δf as an output signal. This signal is fed forward into

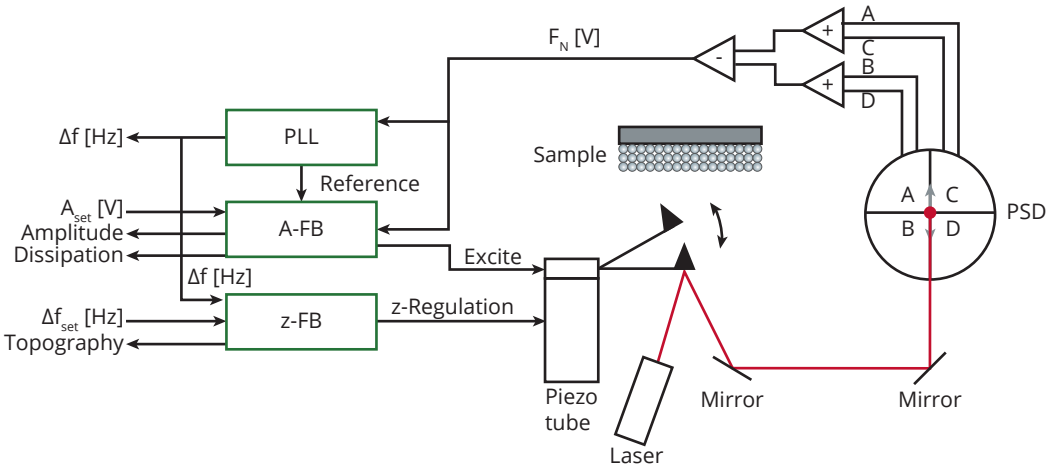

Fig. 2.5.: Basic setup scheme of of an NC-AFM experiment

the electronics for recording and into the distance control circuit. The distance control circuit, subsequently, adjusts the tip-sample distance and records the change, namely the topography.
The F_N signal is further processed by the A-FB and compared with a pre-set, i.e. A_{set}. Additionally, the amplitude (A) and the dissipation (Γ) are recorded. The signal to excite the piezo is then calculated from the product of the A-FB and the PLL.

2.7 KPFM

Since AFM, ideally, maps the topology of a sample surface, no information on the local surface charge distribution can be extracted from the data.[17] To overcome this limitation, Kelvin-probe force microscopy (KPFM) was introduced. FM-KPFM extends the capabilities of SPM, by measuring the contact potential difference (CPD) between a metallic tip and a metallic sample.

The basic principle originates from the historical Kelvin probe,[18] where two metals exhibiting different work functions will transfer charges, until their Fermi levels are aligned. By applying a suitable compensation potential, the equalizing of the Fermi levels can be nullified. This concept was developed further by Zisman in 1932[19] and transferred from the macroscopic to the nanoscopic scale by Nonnenmacher et al. in 1991, by introducing KPFM.[20] For KPFM measurements on bulk insulators, however, the contrast formation is highly complex and still not thoroughly understood. Thus, only the general setup will be discussed here. For a detailed theoretical approach, please see Neff et al.[21]

When a DC voltage U_{DC} is applied in an FM-NC-AFM measurement, the frequency shift Δf of the oscillating cantilever is shifted, due to a change in the electrostatic

interaction (see green curve in Fig. 2.6). In order to minimize the electrostatic interaction, and in consequence the frequency shift, a voltage U_{cpd} has to be applied. In regular AFM experiments, this task is done once at the beginning of the experiment, under the assumption that the change in F_{el} is negligible. In KPFM, however, the applied voltage U_{dc} (red curve in Fig. 2.6) is modulated with an additional AC voltage U_{mod}, having the frequency f_{mod}. This results in a frequency modulation of the cantilever frequency shift Δf, with an amplitude proportional to U_{mod}. The KPFM feedback loop, subsequently, tries to minimize the amplitude of this frequency modulation by varying U_{dc} until $U_{dc} = U_{cpd}$ (grey curve in Fig. 2.6). Thus, tracking the change in U_{cpd}, while the cantilever is scanning the sample surface.

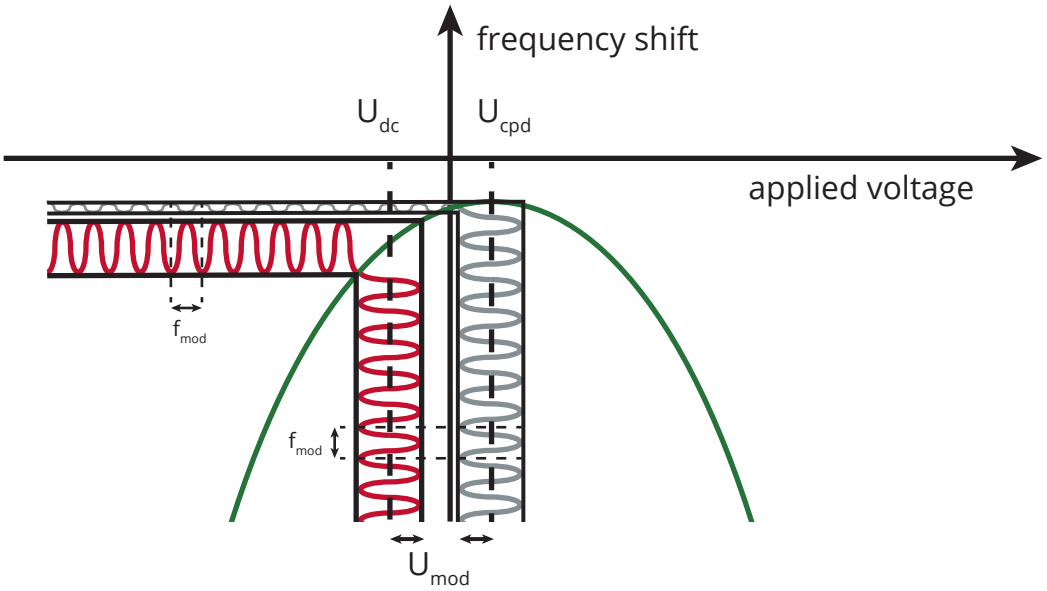

Fig. 2.6.: By sweeping the applied voltage between tip and sample and simultaneous recording of the cantilever frequency shift, the amplitude of the modulation (red curve) along the Y-axis is minimized when $U_{dc} = U_{cpd}$. Adapted from [22].

In typical FM-KPFM experiments $U_{mod} = 2\,\mathrm{V}$ and $f_{mod} \approx 1\,\mathrm{kHz}$.

3 Bulk Insulator Calcite

3.1 Calcium Carbonate

Calcium carbonate ($CaCO_3$) is the most ubiquitous simple salt on earth.[23] It is found as a major component in marine organisms, e.g. plankton, red algae and several sponges. In these organisms, calcium carbonate is combined with numerous organic materials to create structures with outstanding properties, e.g. shells with a significantly higher fracture toughness.[24] It is widely used in industrial applications, e.g. as a filler in plastics, as an additive in acid-free paper.[25] Given the fact that 60% of the world's hydrocarbons are located in carbonate rocks,[26] research on calcium carbonate is of high importance for the oil-producing industry. The outstanding birefringence of calcite makes it useful for e.g. polarizing prisms[27,28] and it can be used to determine the position of the sun with a precision of $\pm 1°$, even through clouds or in twilight.[29] Thus, a deeper understanding of the interaction between organic molecules and calcium carbonate is crucial for countless research fields, ranging from basic research to industrial applications.

In its crystalline form, calcium carbonate has three different polymorphs, namely aragonite, vaterite and calcite. Since calcite is thermodynamically the most stable polymorph, vaterite and aragonite transform into calcite over time. In addition to the natural modifications, five synthetic modifications are described in literature. These modifications, namely calcite I - V, have been synthesized under high-temperature and/or high-pressure conditions.[30] Calcite is a transparent crystal, with a defined Mohs hardness of 3 and a density of $2.71\,\mathrm{g\,cm^{-2}}$.[31] Calcite crystallizes in the trigonal hexagonal crystal system and is described by the space group $R\bar{3}2/c$. Furthermore, being a bulk insulator, it has a band gap of $E_{gap} = 6.0\,\mathrm{eV}$.[32] Hence it is an ideal substrate for future molecular electronic devices, where full electronic decoupling from the substrate is mandatory.

3.2 The (10.4) cleavage plane

The most stable cleavage plane of calcite is the (10.4) plane. This plane has been found to exhibit a significant templating effect on organic molecules.[33–36]

Additionally, it has a surface of energy of $\gamma_s = 590\,\mathrm{mJ\,m^{-2}}$, which is considerably high compared to other bulk insulators, e.g. KBr, NaCl or CaF_2.[37]

As can be seen in Fig. 3.1 (A), the (10.4) surface has a rectangular unit cell with the dimensions $0.5 \times 0.81\,\mathrm{nm}^2$. Moreover, the unit cell consists of two calcium ions and two carbonate groups. Along the $[42\bar{1}]$ direction, the carbonate groups alternate their orientation, resulting in a zig-zag pattern of the protruding oxygen atoms. Since the carbonate groups form an angle of 44 ° to the surface, the oxygen atoms lie 78 pm above or below the plane of the calcium ions. For the calcite (10.4) surface,

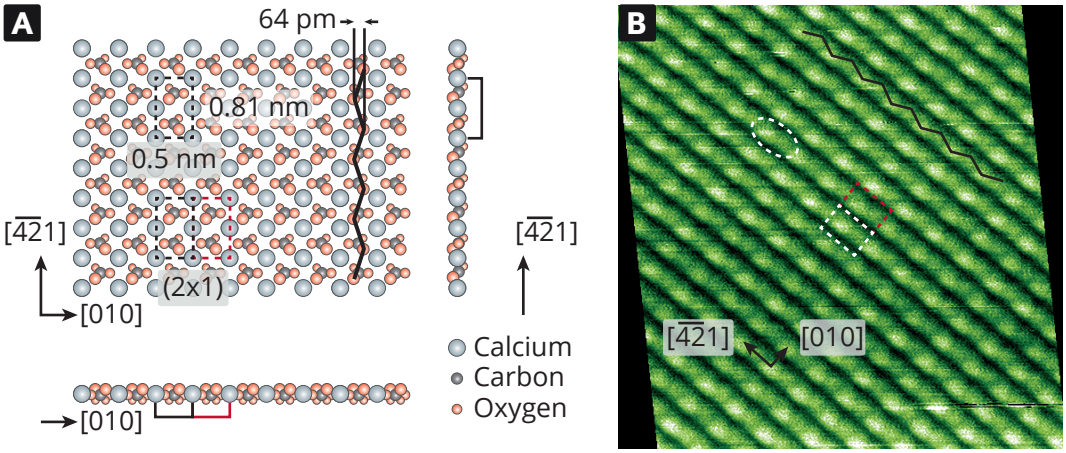

Fig. 3.1.: (A) Model of the (10.4) cleavage plane and the corresponding unit cell.; (B) Drift-corrected NC-AFM image of the bare (10.4) surface of calcite. The surface unit cell and the (2×1) reconstruction are indicated by the white dashed rectangle and the white and red dashed rectangle,respectively. Furthermore, along the $[42\bar{1}]$ direction, the zigzag of the carbonate groups (black line) and the row-pairing (white dashed ellipse) can be observed.

two reconstructions are described in literature (see Fig. 3.1). The first is the (2×1) reconstruction, which was first observed by low-energy electron diffraction (LEED) in 1991.[38] This reconstruction manifests in alternating bright and dark features along the [010] direction (red and white dashed rectangle in Fig. 3.1 (B)). The second reconstruction is the so-called row-pairing (white dashed ellipse in Fig. 3.1 (B)). Here, two neighbouring carbonate groups along the $[42\bar{1}]$ direction slightly differ in appearance, and, thus, give the impression to form a pair. First observations of this contrast were reported for contact AFM in water.[39]

The birefringent nature of calcite allows for an easy determination of the absolute orientation outside of the UHV chamber. If light passes the crystal perpendicular to the (10.4) surface, it is split up along the $[42\bar{1}]$ direction.[5] Thus, the orientation of the crystal examined by AFM can be determined by a complementary method.

A detailed description of the bulk structure of calcite, the peculiarities of the (10.4) surface and a thorough analysis of its contrasts in NC-AFM experiments can be found in the thesis of P. Rahe.[5]

4 On-Surface Synthesis

In recent years, on-surface chemical reactions have proven to be a highly versatile tool for the creation of stable molecular structures.[4,40] As compared to molecular self-assembly, which relies on reversible intermolecular interactions,[41] on-surface synthesis provides the opportunity to create stable molecular structures by formation of covalent bonds. Performing the reactions directly on the surface bears a great potential for surface functionalization and the creation of functional devices, e.g. in the field of molecular electronics. On-surface reactions can be realized without solvents under ultra-high vacuum conditions, which allows for utmost control over the purity of products. Moreover, on-surface synthesis offers the possibility to prepare compounds that cannot be synthesized in solution due to solubility issues. Most importantly, the confinement of the reaction into two dimensions gives access to entirely new reaction pathways, e.g. by stabilizing specific conformers. For the investigation of these reactions, scanning probe techniques are a most valuable tool, since they allow for directly imaging the precursors and their resulting products in real space.
In this chapter, I give an overview of the advances and the current state-of-the-art in this highly active field of research. Starting from proof-of-principle studies at the beginning of this millennium, the consequent enhancement of these reactions will be discussed. Furthermore, concepts improving reaction control, structural complexity and stoichiometry are presented. Finally, first successful approaches towards on-surface synthesis on insulating substrates are shown.

4.1 Proof-of-Principle

Since on-surface reactions can be classified as a new kind of reaction type, already established reaction concepts and reaction procedures have to be thoroughly adapted to fit the modified environment in the presence of a surface. Numerous synthetic protocols have already been transferred and adapted to fit the specific needs of on-surface synthesis.

Among the first examples for the on-surface creation of covalent bonds between molecules is the well-known Ullmann coupling. The classical Ullmann synthesis has first been described in 1904[42] and allows for the selective formation of carbon-carbon

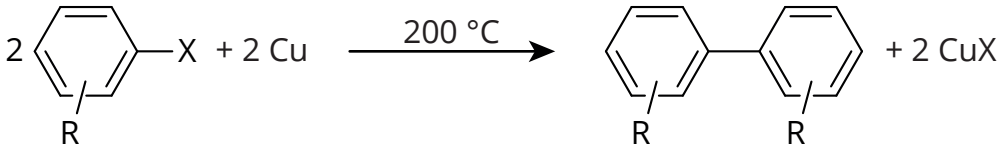

Fig. 4.1.: Cu-mediated Ullmann coupling between two aryl halides.

bonds between two aryls by a Cu-mediated activation of halogen aryls, such as chlorobenzene (see Fig. 4.1).

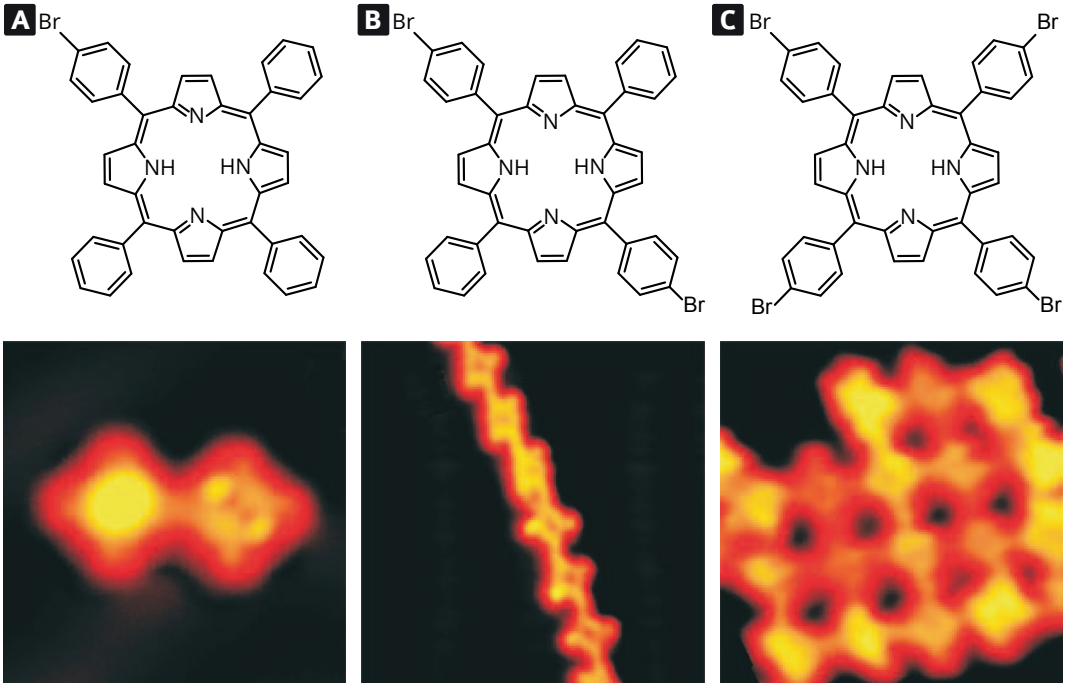

Fig. 4.2.: Ullmann coupling of substituted porphyrins with control over the dimensionality. By using different building blocks with (A) one, (B) two or (C) four Br substituents, dimers, one-dimensional lines or two-dimensional networks are formed (see STM images below). Adapted from [43].

On a surface, this has been demonstrated with scanning tunneling microscopy for the first time by Hla et al. in 2000.[44] In this case, they have adsorbed iodobenzene on a Cu(111) surface held at 20 K. By applying a voltage pulse with the tip of a scanning tunneling microscope (STM), the carbon-iodine bond could be cleaved. Subsequently, two closely lying phenyl radicals have been brought into proximity of each other by lateral manipulation again using the STM tip. With a further voltage pulse, the two phenyl radicals have been covalently linked to form a biphenyl molecule. The successful linkage has been demonstrated indirectly by manipulation of the newly formed molecule that has been moved as an entity. Another prominent example for on-surface synthesis using an STM tip to initiate the reaction is the polymerization of diacetylenes. Aono et al. have been able to initiate the polymerisation of 10-12-nonacosadiynoic acid, adsorbed on a graphite surface, into a polydiacetylene

nanowire. Interestingly, the start of the reaction could be precisely controlled by applying a voltage pulse with an STM tip, while the reaction direction has been governed by the underlying substrate, resulting in uni-directional rows.[45]

Despite the impressive nature of these experimental achievements, reaction initiation by the tip of an STM appears unlikely to be adopted for the creation of extended nanostructures, because of its serial concept. A most promising parallel approach has been published by Grill et al. in 2007.[43] After adsorbing porphyrins with a varying number of bromine substituents on a Au(111) surface, they have been able to deliberately steer the dimensionality of the reaction product. By annealing the gold substrate to 400 K, thermal homolysis of the carbon-bromine bond has been induced and a phenyl radical has been created. During diffusion on the surface, the highly reactive radicals recombined and formed dimers, linear chains or extended networks (see Fig. 4.2). Based on the same strategy, other examples exist in the literature. Lipton-Duffin et al. have demonstrated the coupling of diiodobenzene on Cu(110).[46] By using the two isomers 1,4-diiodobenzene and 1,3-diiodobenzene, they have been able to create poly(para-phenylene) lines and poly(meta-phenylene) zigzag rows, respectively. Additionally, the reaction of 1,3-diiodobenzene has allowed for the formation of sexiphenylene macrocycles. A similar approach has been used by Fan et al. By enlarging the reactant by two meta-positioned phenyl rings, i.e., changing from 1,4-dihalobenzene to 4,4"-dihalo-m-terphenyl, they have been able to synthesize hexagonally-arranged hyperbenzene macrocycles on a Cu(111) surface.[47] Similarly, the synthesis of poly(3,4-ethylenedioxythiophene) by polymerization of 2,5-diiodo-3,4-ethylenedioxythiophene on Cu(110) has been shown.[48] Further example for successful Ullmann-like on-surface syntheses are shown in Table 4.1.

In a comprehensive study comparing various surfaces, Gutzler et al. have shown that the Ullmann coupling crucially depends on the underlying substrate. Thermal annealing of monolayers of 1,3,5-tris(4-bromophenyl)benzene on graphite(001), Cu(111) and Ag(110) has clearly shown that the homolytic cleaving of the C-Br bonds is not taking place on graphite, since the molecules desorb before they are able to react. On metals, however, the split-off Br atoms are chemisorbed to the surface and, in consequence, stabilized.[49] Thus, it is crucial to carefully consider the influence of the substrate on the surface reaction. In this context, metal substrates provide the great advantage that they are catalytically active and typically possess a rather high surface energy.[37]

4.2 Advanced Studies

In the interest of enlarging the set of synthetic tools for the creation of covalent structures directly on the surface, additional chemical reactions have already been

successfully converted into on-surface synthesis concepts. These will be discussed in the following.

4.2.1 Further parallel approaches

C-H bonds are known to be rather inert, especially when considering long alkyl chains. A possibility for activating this bond is the use of aromatic groups or methyl groups added to an aromatic core. Very recently Wiengarten et al. have demonstrated the creation of homocoupled porphine arrays. The activation of the C-H bonds situated directly at the aromatic ring has allowed for the creation of up to three C-C bonds between neighboring molecules.[50] Due to the desorption of molecules upon post-deposition annealing, they have deposited the molecules directly on a surface, held at elevated temperatures. By performing the reaction at different sample temperatures, they have been able to increase the yield of coupled porphine from 70 % at 533K̇, to 99 % at 613 K.

In't Veld et al. have shown an oligomerization of tetra(mesityl)porphyrin.[51] This reaction is facilitated by the fact that the radicals formed when cleaving off one hydrogen atom are comparatively stable. This stabilization is due to the aromatic core of the mesityl groups, which stabilizes radicals by delocalization. Hence, the recombination of the two created radicals is hindered and the porphyrin radicals exists long enough to find a suitable reaction partner. Thus, simple annealing of these precursors on a Cu(110) held at 420-470 K has shown to be sufficient to form covalently linked oligomers. The C-H activation of linear alkanes has been shown by Zhong et al.[52] Deposition of di(eicosyl)benzene (DEB) on a Au(110) surface constrained the molecules into one dimension. Subsequent annealing to 420 K has yielded the corresponding polymer, namely poly(DEB). Calculations have shown that the Au(110) surface lowers the C-H activation energy from $E_a >$ 4 eV to $E_a \approx$1 eV. This work impressively demonstrates that even a rather simple and especially unreactive molecule, if treated correctly, can undergo an on-surface reaction and result in stable surface structures. A very peculiar approach to create fullerene hemispheres has been shown by Rim et al.[53] Using hexabenzocoronene as a precursor adsorbed on a Ru(0001) surface, relatively mild annealing to 380 K has been shown to initiate multiple cyclodehydrogenation reactions, as has been corroborated by H2 temperature-programmed desorption (TPD) spectra. Additional STM images have revealed the conversion of hexabenzocoronene into fullerene hemispheres. This concept has been further explored by Otero et al.[54] They have deposited $C_{60}H_{30}$ and $C_{57}H_{33}N_3$ onto a Pt(111) surface. Upon annealing the substrate to 750 K they have been able to transform the first compound into C_{60} fullerenes and the second compound into a triazafullerene, respectively. Based on the same strategy, Amsharov et al. have been able to synthesize C_{84} on a Pt(111) surface.[55]

A unique decarboxylation reaction has been shown by Gao et al.[56] The deposition and subsequent annealing of naphthalene-dicarboxylic acid on both, Ag(111) and Cu(111), at first resulted in a deprotonation due to the coordination between the carboxylate and the metal. In a second step, CO_2 has been cleaved off, yielding a one-dimensional chain of naphthalene biradicals linked by metal atoms. As a last step, the biradicals recombined in order to form poly-naphthalene wires.

All of the aforementioned reactions, however, rely on the activation of either C-H bonds or C-X bonds, both being single bonds. Diaz Arado et al. have demonstrated the use of aldehyde groups in a McMurry type[57] reductive coupling reaction for the direct synthesis of vinylene groups (see Fig. 4.3).[58] In order to circumvent the desorption of the molecules, before the reaction has taken place, they have followed the strategy of depositing the molecules directly onto the Au(111) substrate kept at 250 C°.

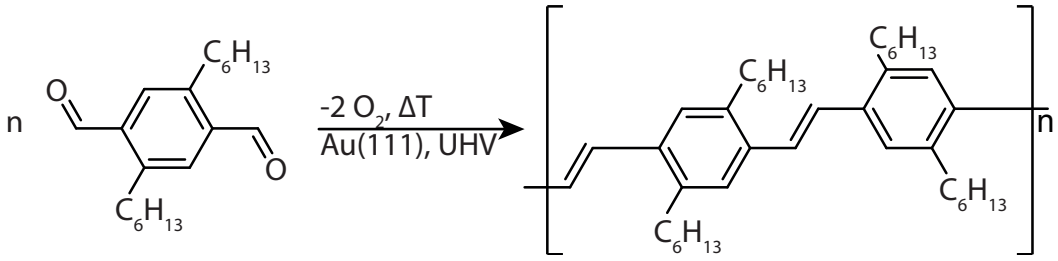

Fig. 4.3.: McMurry type reductive coupling of aldehydes. Adapted from [58]

A non-reductive approach to create double bonds has been presented by Matena et al. Upon deposition of 1,3,8,10-tetraazaperopyrene on a Cu(111) surface, the molecule readily tautomerized into an intermediate *N*-heterocyclic carbene (*N*HC). Subsequently, the *N*HCs recombined to form regular oriented oligomer chains.[59,60] One of the most studied cycloaromatization reactions is the Bergman cyclization.[62] By heating of an enediyne, a highly reactive para-benzyne radical is formed, which yields a benzene ring, if supplied with hydrogen atoms from a donor. This reaction has been shown in a very peculiar way by deOteyza et al.[61] As can be seen in Fig. 4.4, heating of the ethinyl-substituted phenyl rings on a Ag(100) surface has initiated an intramolecular Bergman cyclization, yielding three isomeric products. Furthermore, they have been able to assign all isomers by submolecularly resolved nc-AFM images. The Bergman cyclization has also been used for creating polyphenylene nanowires. For this purpose, Sun et al. have deposited 1,6-di-2-naphthylhex-3-ene-1,5-diyne onto a Cu(110) surface.[63] Instead of saturating the intermediate para-benzyne diradicals with hydrogen, the highly reactive molecules have recombined to yield the respective polyphenylene chains. Since alkynes bear a triple bond, they allow for synthesizing aromatic molecules via cycloaddition. This has been shown recently by Liu et al.[64] By a stepwise reaction scheme of triethynyl benzene on Au(111), they have yielded

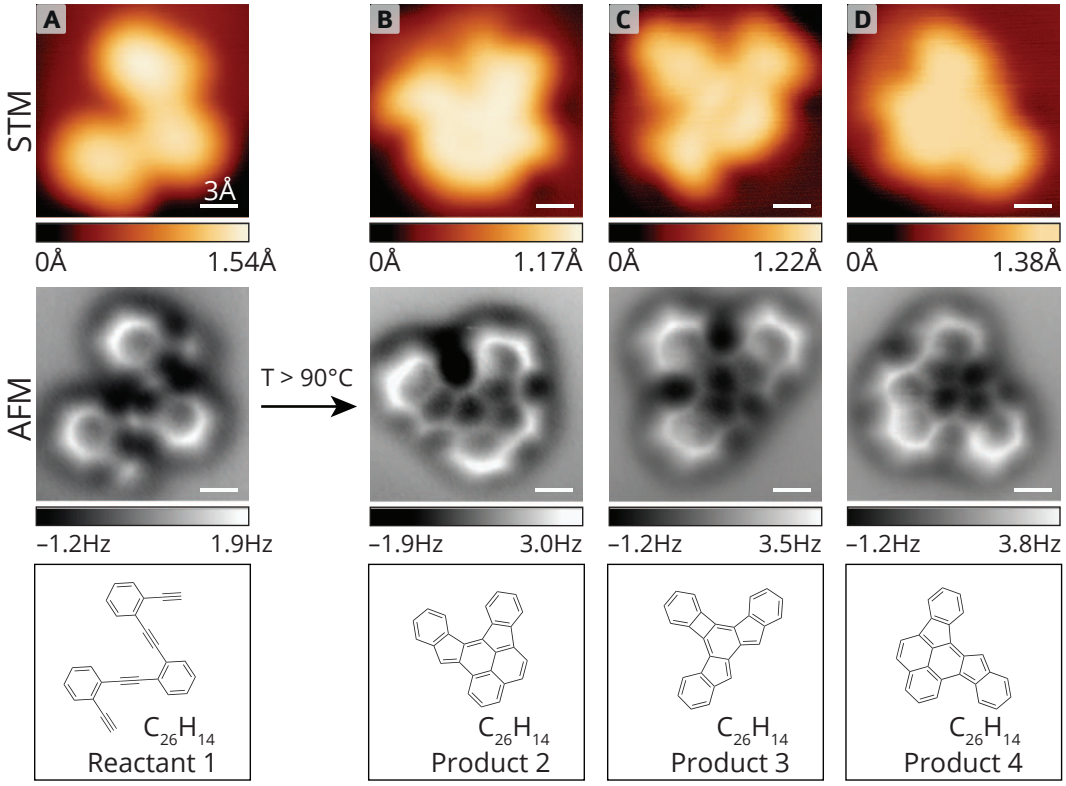

Fig. 4.4.: Bergman cyclization on Ag(100). Upon thermal annealing, the precursor (A) reacts and forms the three isomers (B-D). Adapted from [61]

a two-dimensional polyphenylene network, with a pore size of 1.7 nm. Besides being highly active precursors, as just shown, alkyne groups bear the potential for the creation of rigid and linear nanowires, due to the sp-hybridization of the carbon atoms. In order to covalently link these alkyne groups, chemists have used Glaser-type coupling reactions based on Cu-catalysis for the last 150 years.[65] Very recently, this reaction has been transferred to surfaces by Zhang et al.[66] Unlike the Ullmann coupling previously discussed, the subsequent annealing of the adsorbed molecules has resulted in desorption of 1,3,5-triethynylbenzene molecules, leaving only the Ag(111) bare sample surface. However, by deposition onto the Ag(111) surface, held at 330 K, they have been able to induce dimerization and oligmerization. After this first reaction step, the molecules could be annealed to 370 K, inducing a further oligomerization of the molecules. The on-surface coupling of alkynes has also been shown on Cu(111),[67] Ag(111),[68,69] as well as by photochemical activation with visible light.[56] As discussed for the Ullmann coupling, the substrate has a crucial influence on the reaction. In two comparative studies, Gao et al. have found that on the Ag(111) surface the desired linear coupling product of a bisethynylbenzene was formed with a yield of 64

4.2.2 Sequential activation

In order to gain more control over the reaction, a sequential reaction process has been explored as a highly promising approach for hierarchical covalent linkage. Making use of the differences in bonding strength in halogen-carbon bonds, Grill et al. have been able to steer the degree of polymerization.[70] By exchanging two of the iodine atoms in tetrakis(4-iodophenyl)-porphyrin by bromine atoms, they have been able to exclusively cleave off the iodine atoms in a first annealing step. After the subsequent formation of a one-dimensional polymer, the cleaving of the carbon-bromine bonds has been initiated by a second annealing step. By following this route, they have been able to cross-link the linear polymer rows, obtained in the first annealing step, resulting in an extended two-dimensional network structure with improved degree of order (see Fig. 4.5).

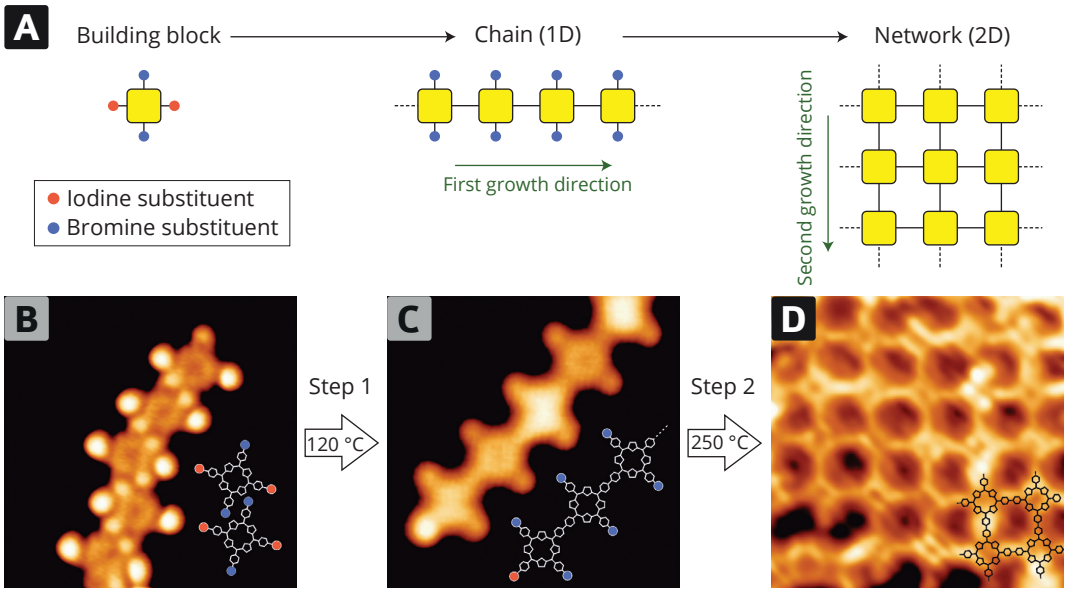

Fig. 4.5.: (A) Two-step activation mechanism of the Ullmann coupling using iodine and bromine substituents; The pristine molecules (B) form linear chains after a first heating step (C), which react further to a two-dimensional network (D); Adapted from [70].

A remarkable example has been shown by combining the Ullmann coupling with a subsequent Scholl reaction.[71] The latter being a coupling reaction between two arene compounds by the loss of hydrogen. Cai et al. have deposited 10,10'-dibromo-9,9'-bianthryl on a Au(111) surface.[72] At first the Ullmann coupling has been initiated by annealing of the substrate to 200 °C. Hereby, the bianthryl units have formed a linear polymer. After a consecutive second annealing step at 400 °C, a linear graphene nanoribbon has been obtained *via* the aforementioned Scholl reaction. Furthermore, depending on the employed precursor, they have been able to precisely choose between zigzag and armchair graphene nanoribbons. Lin et al. have shown the ring-opening polymerization of melamine on Cu(111).[73] By annealing, they have observed two phase changes. At room temperature the pristine melamine molecules

have been found to self-assemble in an upright standing configuration. Upon heating to 420 K, the domains have reoriented into linear chains. Further annealing to 570 K has resulted in the formation of a two-dimensional covalent network.

4.2.3 Reactions involving two reactants

Since it is often not possible or feasible to incorporate all groups necessary for a reaction in a single molecule, reactions involving two reactants have been explored. Such reactions also bear the potential that reaction initiation might occur without the need of annealing, simply by codeposition of the two educt species. Among the first approaches, the condensation reaction of an aldehyde and an amine yielding a Schiff base has been shown by Weigelt et al. on an Au(111) surface.[74] In this work, no annealing was needed to induce this reaction, simply the presence of the two molecules at the surface has been sufficient. By taking the next logical step and using bi- and trifunctional molecules, they, consequently, have been able to form a polyimine network on the same surface.[75,76] Similar reactions shown have been the condensation of primary amines to tertiary amines,[77] the formation of a polyimide[78,79] and the polycondensation using co-sublimated boronic acids and hydroxy-functionalized molecules.[80,81] Furthermore, the condensation between highly reactive acyl chlorides with amines on Ag(111) has shown to yield the respective polyamides.[82–84] Despite being highly valuable synthetic tools, condensation reactions bear one drawback for on-surface synthesis, i.e., the formation of byproducts. The condensation product, e.g., water or even hydrochloric acid, contaminates the surface and can lead to side reactions or other undesired effects. Thus, addition reactions, which yield no byproducts per definition, have been investigated for on-surface synthesis. As an example for an addition reaction, melamine, an aromatic triamine, has been studied by Jensen et al.[85] This molecule readily reacts with 1,4-phenylene diisocyanate on a Au(111) surface to form polyurea networks. Mild annealing has shown to further accelerate the polymerization by disrupting the close-packed melamine domains.

The well-known Huisgen 1,3-dipolar cycloaddition is a very versatile method for the creation of 1,4-triazoles in standard organic chemistry (see Fig. 4.6).[87] Here, an alkyne and an azide undergo a Cu-catalyzed cyclization in an atom economic reaction. Because of the high yields and the inherent atom economy, it falls under Sharpless' definition of "click" chemistry.[88] Bebensee et al. have been the first to transfer this reaction to a Cu(111) surface.[86] By cosublimation of 9-ethynylphenanthrene and 4-azidobiphenyl, it has been found that these two compounds react already at room temperature to yield the corresponding triazole. Similarly, Diaz Arado et al. have shown an oligomerization approach on Au(111), where the azide and the alkyne were situated in the same molecule.[58] Furthermore, the formal [2+2] cycloaddition

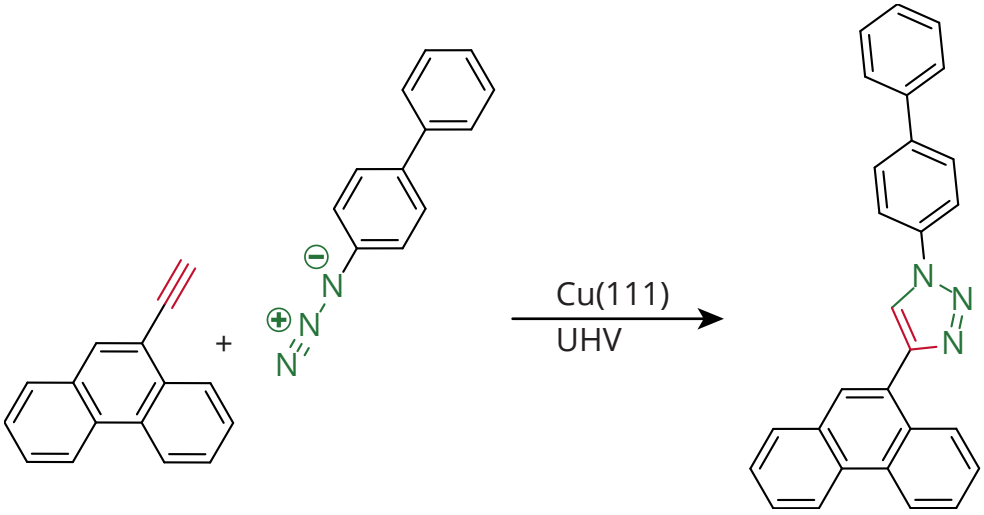

Fig. 4.6.: Huisgen 1,3-dipolar cycloaddition between 9-ethynylphenanthrene and 4-azidobiphenyl. Adapted from [86].

between an alkyne-substitued porphyrin and 7,7,8,8-tetracyano-p-quinodimethane (TCNQ) has been shown by Fesser et al.[89]

4.3 Reactions on Insulating Substrates

Metals typically possess a higher surface energy than most insulators,as evident from the values in Tab. 4.2.

As discussed above, metal surfaces exhibit several advantages for on-surfaces synthesis. First, organic precursor molecules typically anchor firmly to metal surface, permitting the use of annealing as a straight-forward reaction initiation. Second, metals surfaces have been shown to promote the on-surface reaction by acting as a catalyst.[49] Extending the possible substrates to electrically non-conducting surfaces is, however, of fundamental interest to provide maximum flexibility for future applications. Most importantly, when considering on-surface synthesis for molecular electronics applications, the molecular electronic structure needs to be decoupled from the underlying substrate, which is not the case when using metallic substrates. Hence, exploring reactions on thin insulating films and, especially, bulk insulators is of utmost importance. First reactions on thin insulating films, supported by a metallic substrate, have been realized by Abel et al.[111] By using a very common route for the synthesis of metallophthalocyanines, they have been able to synthesize two-dimensional networks. By depositing 1,2,4,5-tetracyanobenzene and Fe in a ratio of 2:1, the phthalocyanine network has been formed spontaneously at room temperature on a Ag(100) surface. Although the surface has in advance been partially covered with NaCl islands, the educts have favoured adsorbing on the metal due to a higher molecule-substrate interaction. Only after the metallic parts had been covered with

Tab. 4.1.: Overview of successfully established on-surface reactions under UHV.

Reaction name	Stimulus	Substrate and reference
Ullmann coupling	Δ T	Cu [44, 46–49, 90–93], Ag [49, 72, 93–98], Au [43, 70, 72, 92, 97, 99–102], $CaCO_3$ [34, 103, 104], HOPG [49], NaCl@Au [105], h-BN@Ni [106], graphene@Ni [106]
Ullmann coupling	hν	Sapphire [107], HOPG [108]
Glaser coupling	Δ T	Cu [67, 109, 110], Ag [56, 66, 68, 69, 109, 110], Au [109, 110]
Glaser coupling	hν	Cu [56], Ag [56], Au [56]
Bergman cyclization	Δ T	Cu [63], Ag [61]
Huisgen cycloaddition	Δ T	Cu [86], Au [58]
Scholl reaction	Δ T	Ag [50, 51, 72], Au [52, 72], Pt [54, 55] Ru [53], HOPG [108]
*N*HC Oligomerization	Δ T	Cu [59, 60]
Condensation reaction	Δ T	Au [74–79], Ag [80]
Carbonyl-analogue Addition	Δ T	Au [85] Ag [111], NaCl@Ag [111]
McMurry reaction	Δ T	Au [112]
$[2+2+2]$ Cycloaddition	Δ T	Au [64]
$[2+2]$ Cycloaddition	Δ T	Au [89]
Decarboxylative polymerization	Δ T	Cu [113], Ag [113]

molecules, the molecules formed a two-dimensional network on the NaCl islands, again illustrating the typically weak molecule-surface interaction in case of non-metallic surfaces. The basic reaction for the phthalocyanine synthesis is, as the Huisgen cycloaddition, atom economic, and, thus, no contaminations are produced on the surface. The real value of this synthesis is the potentially exchangeable metal atom, which allows the networks to be adapted to specific requirements. The drawback, however, of these thin insulating films is that the molecules are not fully electronically decoupled from the substrate. This is evident from the ability to perform scanning tunnelling spectroscopy on top of such islands.[105] Thus, it is mandatory to extend the materials' base of the supporting surface to the heterogeneous class of bulk insulators. For these substrates, specific anchoring strategies have to be developed to compensate for the lower surface energy of the substrate. The interaction between the molecule and the substrate can be increased by introducing certain side groups in the molecules, by matching the molecule dimensions with the substrate periodicity and by increasing the number of functional groups.[33]

Tab. 4.2.: Surface energies for various substrates.

Substrate	Surface	Energy / $mJ \cdot m^2$	Reference
C_{60}		116	[114]
KBr	(100)	141	[115]
NaCl	(100)	181	[115]
CaF_2	(111)	480	[116]
$CaCO_3$	(10.4)	590	[117]
Ag	(110)	1299	[118]
Au	(111)	1506	[119]
Pt	(111)	2299	[119]
Ru	(0001)	3043	[119]

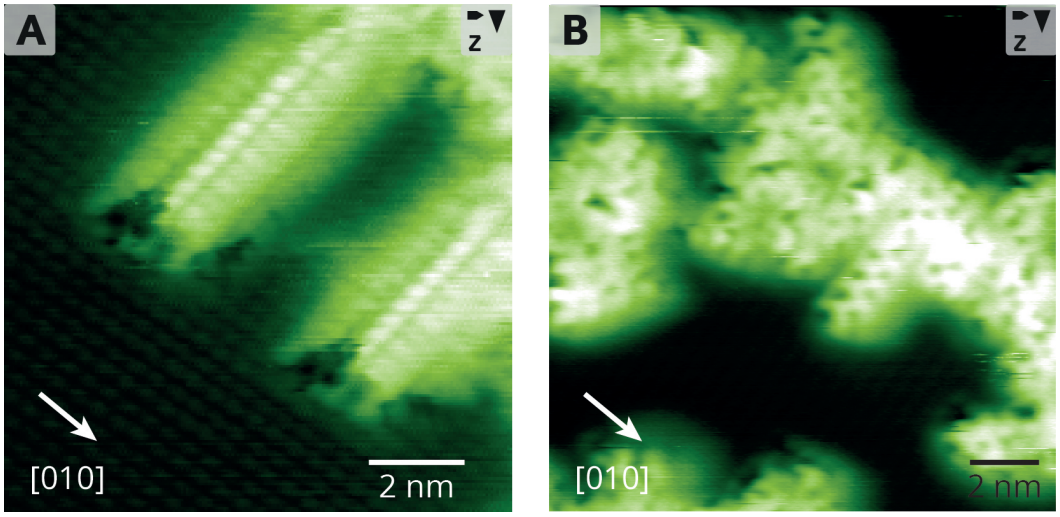

Fig. 4.7.: Thermally initiated Ullmann-type coupling of (A) diiodobenzoic acid and (B) diiodosalicylic acid. Adapted from [103].

As a first example of an on-surface reaction on a bulk insulator substrate, Kittelmann et al. have explored Ullmann-type coupling on $CaCO_3$ (10.4), calcite. On $CaCO_3$, carboxylic acid groups have proven to be valuable functional groups in order to anchor the molecules to the surface.[34,104] Thus, for a simple proof-of-principle 4-iodobenzoic acid (4-IBA) has been chosen. This compound possesses a carboxylic acid group for anchoring to the surface, and a thermally cleavable carbon-iodine bond. Upon adsorption of 4-IBA on $CaCO_3$ and subsequent annealing above 520 K, molecular species have been obtained that fit in size with the expected reaction product, namely 4,4'-biphenyldicarboxylic acid (BPDCA). This on-surface reaction step has been further corroborated by separate deposition of ex-situ synthesized BPDCA.[103] In order to obtain linear polymers, two reactive groups have to be present in para position. Consequently, 2,5-diiodobenzoic acid has been studied on $CaCO_3$. After deposition and subsequent annealing of the substrate above 530 K one-dimensional molecular rows have been revealed, aligned perpendicular to the [010] substrate direction (see Fig. 4.7 (A)). Accordingly, when adsorbing

3,5-diiodosalicylic acid onto the same surface, a zigzag pattern can be observed after thermal annealing (see Fig. 4.7 (B)). Thus, even the shape of the reaction product could be controlled by varying the positions of the reactive sites. Inspired by the

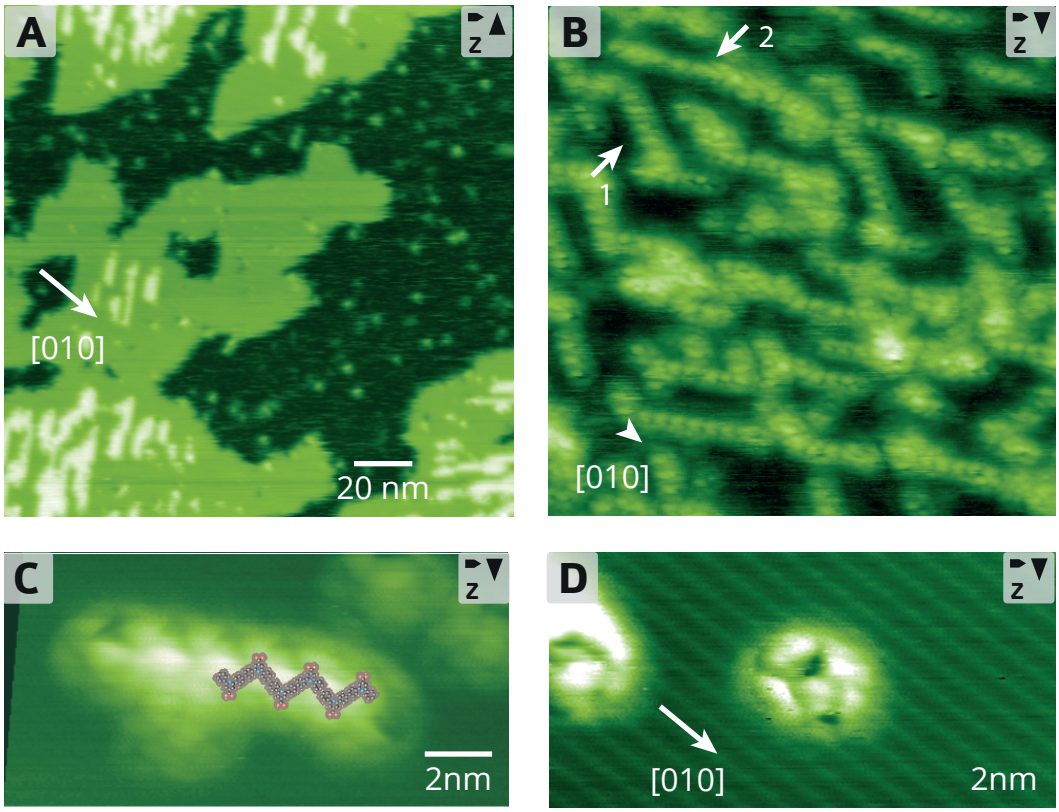

Fig. 4.8.: Site-specific and sequential on-surface reaction on the (10.4) surface of calcite. (A) Islands of BPCPPCA deposited onto calcite(10.4) (B) After a first annealing step to 570 K rows along specific surface directions are observed. (C) After a second annealing step at 610 K, zigzag chains are observed on the surface. (D) Additionally, ring-like structures can be observed. Adapted from [104].

sequential activation strategy first demonstrated by Grill et al.,[70] Kittelmann et al. have extended the above reaction route by using a benzoic acid derivative with two different halogen atoms, namely 2-(4-bromophenyl)-6-(4-chlorophenyl)pyridine-4-carboxylic acid (BPCPPCA). This precursor has been chosen as it bears the potential for a site-specific, two-step reaction on the bulk insulator calcite.[104] After deposition of BPCPPCA molecular islands with a (2×4) superstructure have been observed on the surface (see Fig. 4.8 (A)). This structure is changed drastically after a first annealing step to 570 K. Now, the molecules have formed row-like structures, presumably induced by the cleaving of the C-Br bonds (see Fig. 4.8 (B)). A second qualitative change has been induced by annealing the substrate to 610 K (see Fig. 4.8 (C)). This change is explained by homolysis of the C-Cl bonds, allowing for the formation of extended zigzag and closed ring structures (see Fig. 4.8 (D)).

The above mentioned examples on calcite all rely on the thermal initiation of an Ullmann-type of reaction. This rises the fundamental question as to why the reaction

could be initiated even in the absence of a metal catalyst. A definite answer to this question is lacking at present, however, it appears possible that the strong anchoring of the molecule towards the calcite surface weakens the C-halogen bond and, thus, favours homolytic cleavage of this bond. From a fundamental point of view, it would be most desirable to explore other means of reaction initiation than thermal activation. This is especially true for insulating surfaces to reduce the risk of desorption upon reaction initiation. But also for decoupling the deposition from the initiation step, it is highly important to explore photochemical initiation as activation step for on-surface synthesis.

4.4 Outlook

On-surface synthesis shows great promise for creating functional molecular structures at surfaces. When compared to self-assembly, on-surface synthesis outperforms in terms of structural stability and specific materials properties such as electron transport. Moreover, this emerging concept allows for preparing compounds that might not be accessible by a classical, solution-based approach due to poor solubility of the involved species. As a most exciting perspective, the two-dimensional confinement of the educt molecules on the surface can be deliberately employed for stabilizing transient structures, which offers the potential to explore entirely new reaction pathways. Fully exploiting the benefits of on-surfaces synthesis will require detailed insight into the chemical nature of the molecule-surface interaction and the specific adsorption geometry. Scanning probe microscopy techniques performed in ultra-high vacuum have proven to provide most detailed real-space information, which has greatly advanced this rapidly growing field of research.

5 Experimental

5.1 UHV system

All experiments were performed in a commercial UHV system (Omicron Nanotechnology, Taunusstein, Germany) with a base pressure $\leq 10^{-10}$ mbar. The system consists of three chambers. The chamber on the right houses the AFM, while the chamber on the left is used for sample preparation. Additionally, a load-lock allows for the lock-in of samples and cantilevers without breaking the vacuum. Attached to the system are a quadropol mass spectrometer eVision+ (MKS Instruments, Andover MA, USA) for the analysis of residual gases, molecule sublimators and a ISE10 sputter gun (Omicron Nanotechnology). The whole system is resting on active damping legs to prevent mechanical noise in the measurements. A photographic image is depicted in Fig. 5.1.

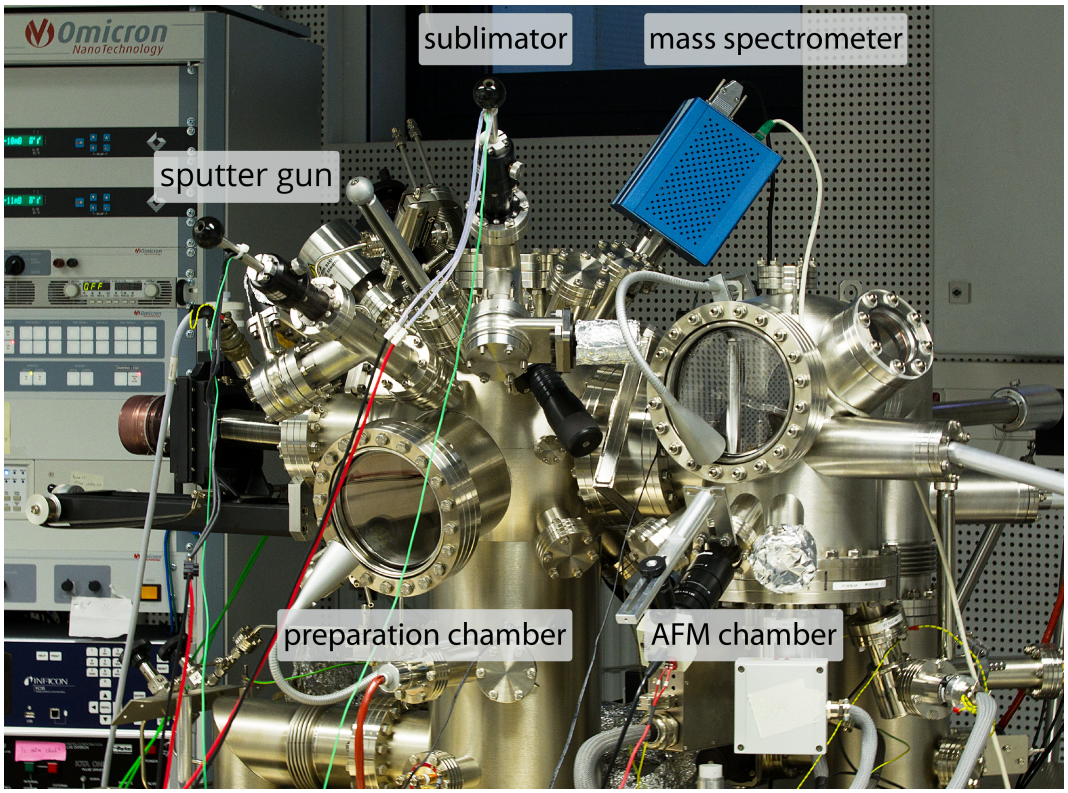

Fig. 5.1.: Setup of the UHV system.

Inside of the AFM chamber a VT-AFM XA (Omicron Nanotechnology) was mounted (see Fig. 5.2 (A)). For a complete decoupling of the AFM stage, it is suspended on springs and equipped with an eddy current damping system. For measurements below room temperature Cu coolin braids connect the sample stage to a flow cryostat, which allows for the cooling with liquid N_2 or He. A close-up of the cantilever, the sample and the piezos are displayed in Fig. 5.2 (B).

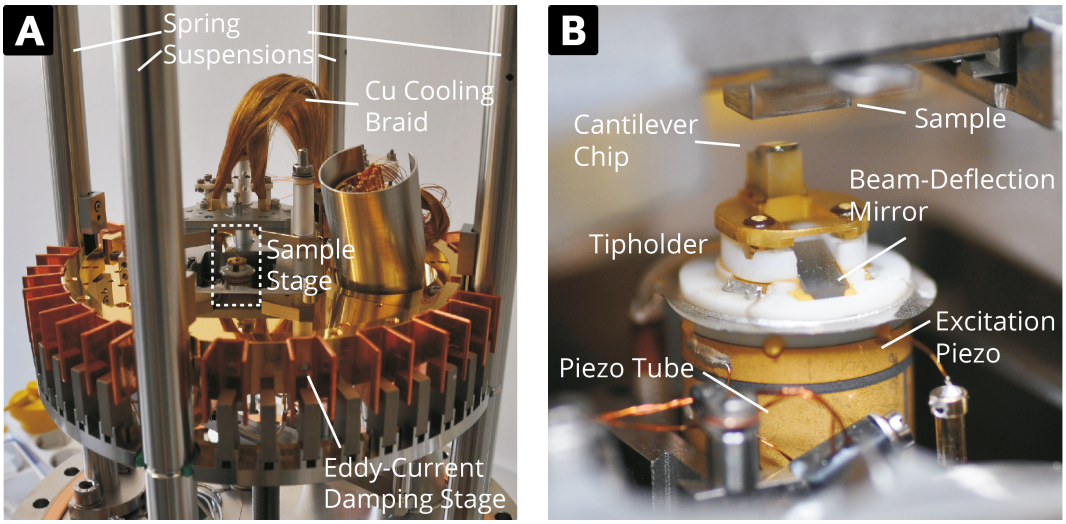

Fig. 5.2.: (A) Image of the VT-AFM XA; (B) Close-up of the scan head.

5.2 Sample preparation

Calcite crystals of optical quality from Korth Kristalle GmbH were mounted in a sample holder. After determination of the absolute crystal orientation using a polarisation filter, the crystals were locked into the UHV chamber over night. Subsequently, they were degassed for 2 h at about 260 °C and cleaved in vacuum to get a clean surface. After repeated heating to 200 °C for 1 h to remove surface charges, the surface was investigated by AFM to assure a clean surface and to verify the crystal orientation.
For the preparation of molecule layers, the compounds were sublimated from a home-built Knudsen cell. As can be seen in Fig. 5.3, the Knudsen cell consists of glass crucible holding the molecular material. In order to prevent the molecular material from falling out, a piece of glass wool is inserted into the top of the crucible. A Ta-wire is wrapped around the crucible to heat the sample. For reading the temperature, a NiCr/Cr-thermocouple is melted into the bottom of the crucible.

For the irradiation experiments, a laser diode having a wavelength of 405 nm and a power of 27 mW (see Fig. 5.3 (B)) was used. The diode was mounted ex-situ, in front of a viewport.

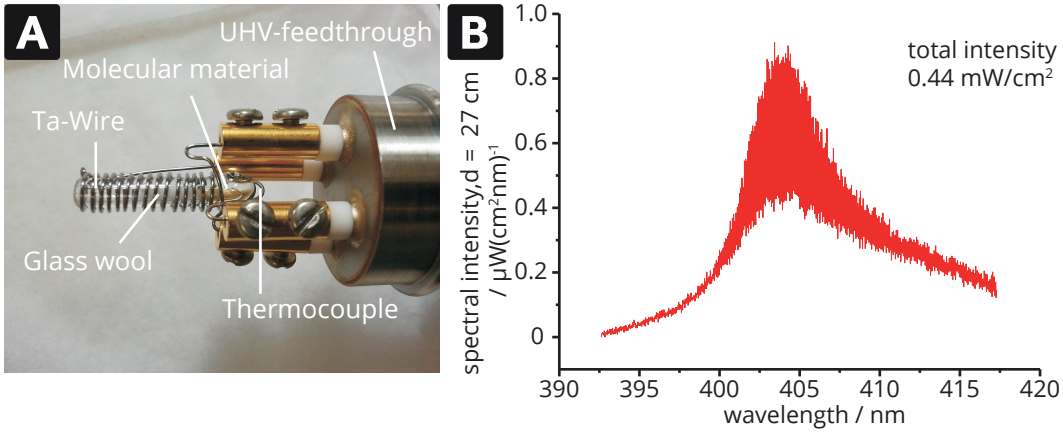

Fig. 5.3.: (A) Setup of the sublimation cell; (B) High resolution spectrum of the laser diode.

Tab. 5.1.: Typical sublimation parameters for the compounds discussed in this thesis.

Compound	T / K	Rate / ML·min^1
C_{60}	645	0.06
PTCDA	461	0.01
TCPTCDA	450	0.01
Cs	4 A	0.25

Sublimation parameters for each compound were determined with a quartz-controlled micro-balance (QCM)(Inficon, East Syracuse NY, USA), by recording the sublimation rate with respect to the temperature. Typical sublimation parameters are given in Tab. 5.1. Please note, for the Cs evaporator no temperature could be recorded because of its construction. Hence, the applied current is given.

5.3 Data Acquisition and Processing

The data were acquired with a VT-AFM-XA , operated in the frequency modulation non-contact mode. The system was equipped with an easyPLL Plus phase-locked loop controller and detector (Nanosurf, Liestal, Switzerland). KPFM measurements were carried out in the frequency modulation mode. For this, a digital lock-in amplifier (HF2LI from Zurich Instruments AG, Zurich, Switzerland) with built-in feedback loop was used. The AC voltage with an amplitude of 2.3 V and a frequency of approximately 1 kHz. By applying the AC voltage to the tip, the resulting electrostatic force is compensated for with an offset DC voltage, i.e. the Kelvin signal. The cantilevers used were n-doped silicon cantilevers (NanoWorld, Neuchâtel, Switzerland) with an eigenfrequency of about 300 kHz (type PPP-NCH) and a Q-factor in UHV of about 20 000. Prior to use the cantilevers were sputtered with Ar^+ at 2 keV and 4.4×10^{-6} mbar for 5 min to remove contaminants.
If necessary the data were corrected for drift using a specifically designed algorithm (see App. C), taking into account lateral and vertical drift,[35] and sample

tilt.[120] Image analysis was carried out under usage of the open-source software Gwyddion.[121] For the case of C_{60}-C_{60} distance histograms (see Chap. 7) a sepcially designed MatLab algorithm was used to evaluate the distances (see App. B).
The AFM data are displayed in such a manner that bright spots resemble large attractive interaction and dark spots resemble low attractive or even repulsive interaction.[122] Furthermore, for all AFM and KPFM images the colour scales in Fig. 5.4 (A) and (B), repectively, were used.

Fig. 5.4.: Colour scales used for (A) AFM and (B) KPFM images

6 Perylene Derivatives on Calcite(10.4)

6.1 Introduction

Molecular self-assembly relies on a fine balance between the molecule-substrate interaction, the intermolecular interaction as well as the diffusivity on the surface.[41] Hence, even small changes in the molecular structure can result in very different self-assembly behaviours, as has been shown for terephthalic acid (TPA)[123] and 2-bromoterephthalic acid (2-BrTPA).[124] At room temperature and submonolayer coverages, TPA molecules on calcite diffuse rapidly on the surface, making it impossible to image them with an AFM. If equipped with a Br moiety, however, the molecules readily occupy stable adsorption positions. In this capter, the concept of providing an anchor functionality is transferred to perylene derivatives. Perylenes are of particular interest for molecular electronic applications, due to their electron transport properties.[125–128] From the numerous derivatives synthetically available, thin films of PTCDA have been thoroughly studied on numerous metals,[129–131] as well as on alkali halides.[132–135] In these studies, PTCDA has shown to form structures ranging from extended wetting layers[131] to bulk-like growth induced by dewetting.[134]

In the following, the adsorption behaviour of PTCDA and TCPTCDA (see Fig. 6.1) on $CaCO_3$ (10.4) will be discussed and compared.

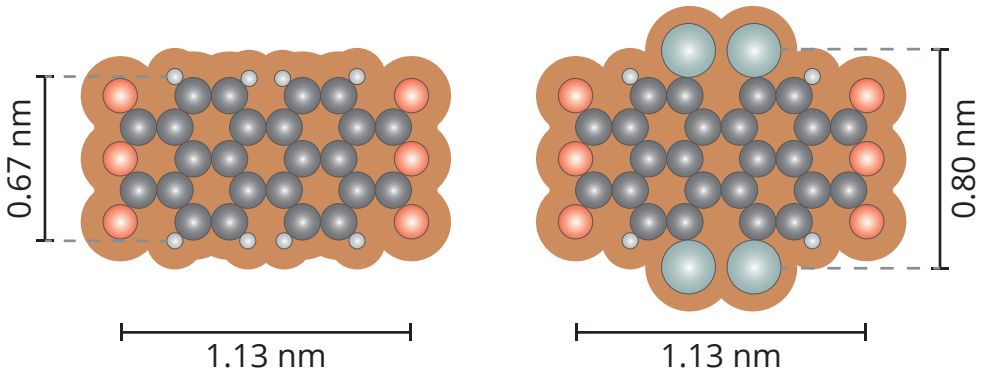

Fig. 6.1.: Molecular structure of 3,4,9,10-perylenetetracarboxylic dianhydride (PTCDA) and 1,6,7,12-tetrachloro-3,4,9,10-perylenetetracarboxylic dianhydride (TCPTCDA), with their respective dimensions.

6.2 PTCDA on Calcite

Upon deposition of PTCDA onto the bare calcite (10.4) cleavage plane, no islands or crystallites can be observed. However, dark features matching the dimensions of PTCDA are observed (see Fig. 6.2). When comparing the two consecutive images in Fig. 6.2 (A) and (B), it can be seen that the molecules diffuse on the surface on a time-scale of minutes. This is particularly evident when looking at the group of molecules marked by the red arrow. While the horizontally aligned group of molecules does not change, the vertically oriented group loses two molecules at the lower end. The inset in Fig. 6.2 (C) is a close-up of the region marked by a red square in Fig. 6.2 (B). Here, the individual molecules as well as the calcite pattern are visible. It can be easily seen that the molecules are oriented parallel to the [010] substrate direction, as shown in the corresponding model.[a] The preferred orientation is evident from the fact, that the O-O distance in PTCDA of $d_{ptcda} = 1.13\,\text{nm}$, matches the 1.5 fold calcium periodicity along the $[42\bar{1}]$ direction, i.e. $d_{1.5Ca} = 1.22\,\text{nm}$, very well. This distance matching results in an attractive interaction between partially negatively charged anhydride groups and the positively charged calcium ions.

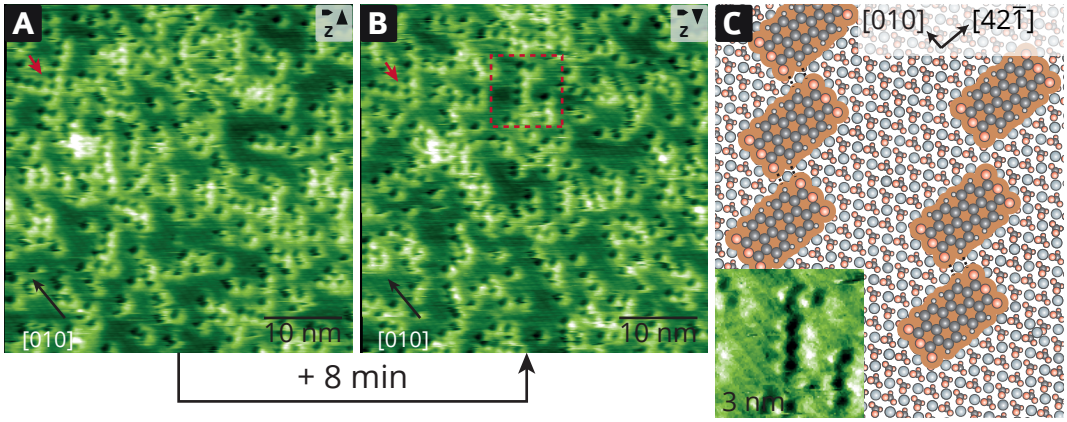

Fig. 6.2.: (A) & (B) Two consecutive images of PTCDA adsorbed on $CaCO_3$ (10.4), showing the diffusion of the molecules. The group of molecules marked in red can be found in both images; (C) Adsorption model of PTCDA. The molecules prefer an orientation along the [010] substrate direction, as evident from the inset.

These findings are in sharp contrast to submonolayer coverages of PTCDA on other substrates. On Cu(111) PTCDA adsorbs in a herringbone-like structure,[130] while on NaCl(100) the molecules favour a commensurate quadratic unit cell. In both cases, however, the molecules in the unit cell adapt two orientations with an angle of circa 90°. This allows all anhydride groups to form hydrogen bonds with the H atoms on the perylene core. For the case of PTCDA on $CaCO_3$, only few hydrogen bonds can be formed (see dashed black lines in Fig. 6.2 (C)). However, due to the

[a] The fact that the molecules in these images are observed as dark spots is explained by the distance-dependent tip-sample interaction.[122] This interaction is the actual measurement signal in NC-AFM experiments.

constructive interaction with the Ca^{2+} ions, the orientation along the [010] direction is favoured, since a rotation by 90° would force one anhydride group of the molecule to be situated closer to a negatively charged carbonate group.

6.3 TCPTCDA on Calcite

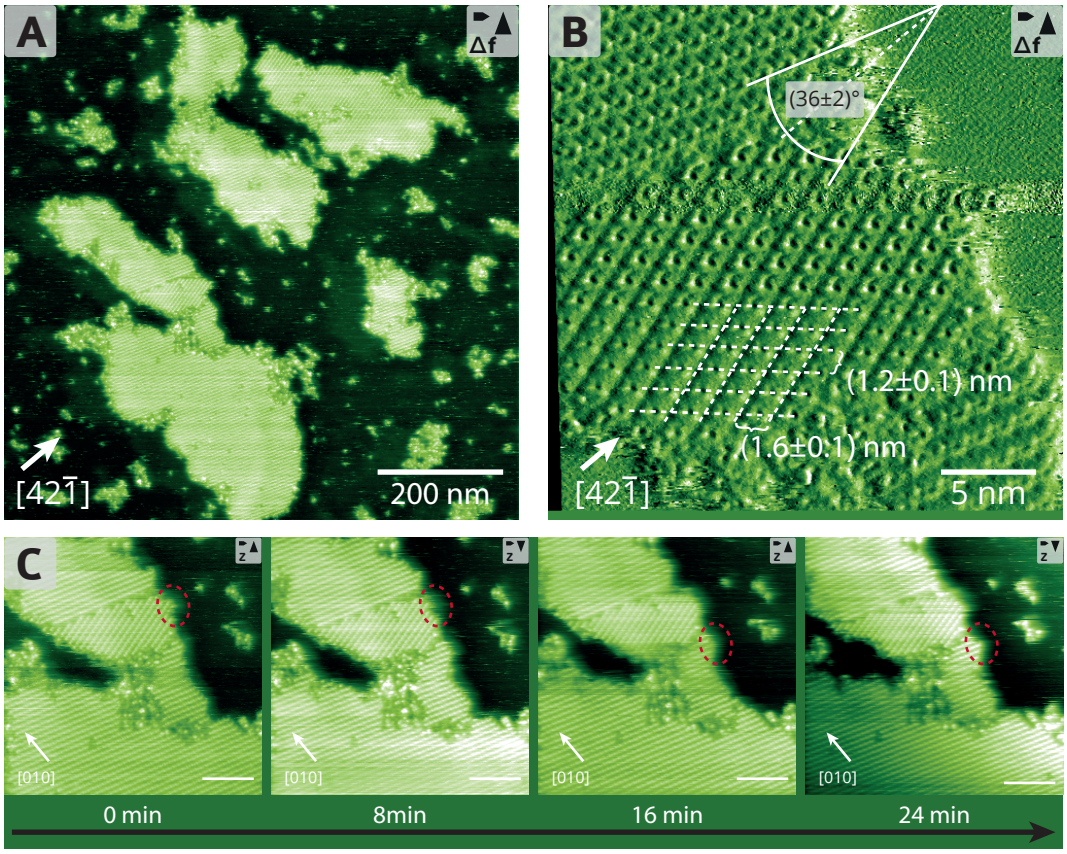

Fig. 6.3.: TCPTCDA adsorbed on $CaCO_3$ (10.4). (A) On a larger scale molecular islands are observed, with stripes in two directions. (B) Molecular resolution reveals two mirror symmetric domains, oriented along the [42$\bar{1}$] substrate direction. The extracted periodicites are (1.2±0.1) nm and (1.6±0.1) nm, as indicated by the white dashed lines. (C) Four consecutive images show that over a total time of 24 min only very few molecules diffuse from and attach to the islands (red dashed ellipse).

Although the substitution of four hydrogen atoms against chlorine atoms does not alter the molecular dimensions too much, the changes in self-assembly behaviour are drastic. Figure 6.3 (A) shows an overview of approx. 0.5 monolayer (ML) of TCPTCDA on $CaCO_3$. In sharp contrast to the previously discussed PTCDA, molecular islands are observed. As can be already seen in the overview, the molecules form two different domains. This is particularly evident in Fig. 6.3 (B), where both domains and the calcite lattice are visible. The two domains consist of rows tilted by 19±1 °, with respect to the [42$\bar{1}$] substrate direction, yielding an angle of 35±2 ° between the rows of the two domains. This is already a strong indication for the formation of mirror symmetric domains, with the [42$\bar{1}$] direction being the mirror

axis. The rows within a domain have a distance of 1.6±0.1 nm. In these rows the periodicity is 1.2±0.1 nm, as indicated by the white dashed lines. Figure 6.3 (C) shows four consecutive images, recorded over a timespan of 24 min. In the island, both previously described domains can be observed. When looking at the upper part of the island (red ellipses) it can be seen that, in contrast to the unchlorinated species, only very few molecules are able to detach and attach to the island on the time-scale of several minutes. With these observations, a model of the self-assembled

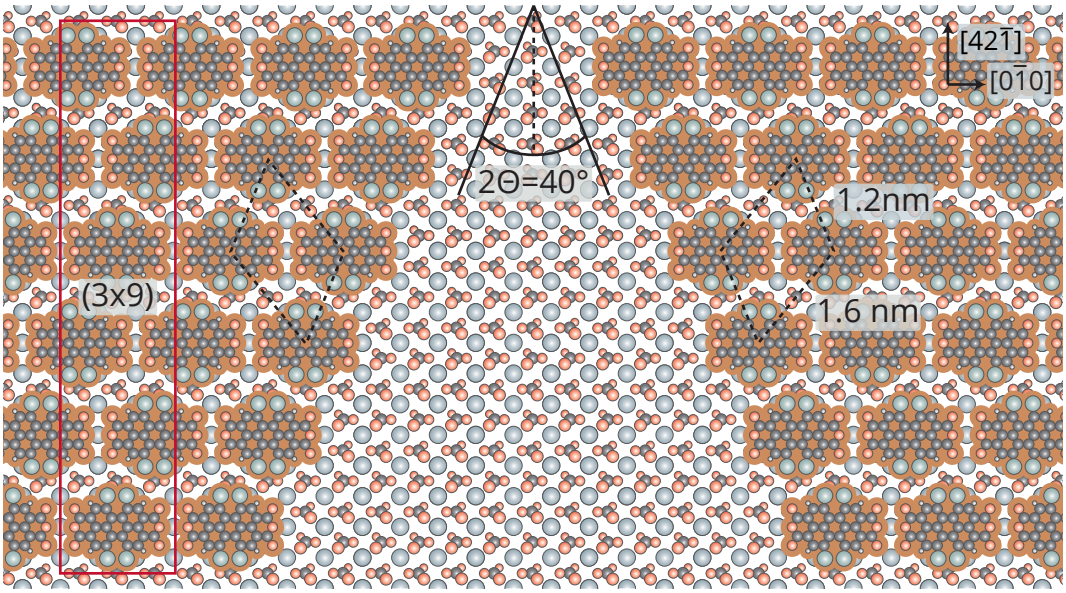

Fig. 6.4.: Adsorption model of TCPTCDA on $CaCO_3$ (10.4). The molecules form two mirror symmetric domains, tilted by an angle of $\Theta = 19°$ with respect to the [42$\bar{1}$] substrate direction. Each row is shifted by 0.5 nm along the [010] substrate direction, resulting in a (4×8) superstructure on calcite.

structure of TCPTCDA on $CaCO_3$ (10.4) can be proposed (see Fig. 6.4). The black rhomb indicates the orientation and the dimensions of the white stripes from Fig. 6.3 (B). Along the [42$\bar{1}$] direction, each row of molecules is shifted by 0.5 nm with respect to each other. This correlates to one unit cell periodicity along the [010] substrate direction. Thus, the molecules form a (3×9) superstructure. The calculated angle in this structure is $2\Theta = 40°$, which is in excellent agreement, with the previously determined value of $2\Theta = 38 \pm 2°$. All molecules occupy equivalent adsorption positions. However, when comparing the structure with the previously analysis of PTCDA, it can be seen that the TCPTCDA molecules are oriented along the [42$\bar{1}$] direction, i.e. perpendicular to the observed orientation of PTCDA. This different orientation is readily explained when considering that the negatively polarized groups, namely the chlorine atoms and the anhydride groups, compete in adsorbing as close as possible to the positively charged Ca^{2+} ions. In the case of PTCDA, this is only possible by orienting the molecule parallel to the [010] substrate direction. For TCPTCDA, however, the distance between the chlorine atoms (d(Cl-Cl) = 0.80 nm) excellently matches the substrate unit cell along [42$\bar{1}$]. Thus, the

molecule is forced into a new adsorption structure. Although this orientation is attained at the expense of constructive interaction of the anhydride groups with the Ca^{2+} ions, the increased interaction of Cl and Ca^{2+} ions is expected to stabilize the molecule in its adsorption position. Furthermore, the introduction of chlorine atoms as additional polarizable groups enhances the intermolecular interaction, and, thus, the formation of islands is favoured.

6.4 Conclusion

In summary, I present a comparison between the self-assembly behaviour of two perylene derivatives, namely PTCDA and TCPTCDA. For PTCDA single molecules, solely oriented along the [010] substrate direction were observed. Furthermore, the molecules readily diffused on the substrate on a time-scale of minutes. For TCPTCDA, however, the observations were significantly different. The molecules self-assembled into large and stable islands. These islands consisted of mirror symmetrical domains, oriented along the $[42\overline{1}]$ substrate direction. I.e. the chlorinated molecules were found to be perpendicular to the unchlorinated species. The difference in adsorption behaviour is readily explained by a change in the dimensions of the molecule. Furthermore, the island formation was attributed to an increased intermolecular interaction, stemming from the chlorine atoms acting as an electrostatic anchor.

These results demonstrate the great potential of rationally designed molecules for deliberately steering molecular self-assembly by exploring the fine balance between the involved interactions.

C_{60} on Calcite (10.4)

7

7.1 General Remarks About Fullerenes

Fullerenes, among which is C_{60}, constitute one of the known allotropes of carbon.[a] The C_{60}-fullerene was first proposed by E. Osawa in 1970,[138] after the synthesis of the bowl shaped corannulene (Fig. 7.1 A). Yet, the first experimental proof was not obtained until 1985, when Kroto and Smalley vaporized carbon clusters from a graphite bulk, using a pulsed laser.[139] They mostly detected clusters with $40 < n < 190$ carbon atoms, with n being an even number. Upon varying the helium flow, they varied the number of collisions between helium and carbon-clusters and managed to favor the accumulation of the extremely stable C_{60}- and C_{70}-clusters.[139,140] The name "fullerene" was chosen by Kroto and Smalley, because the molecule resembled the architectonic style of Richard Buckminster Fuller's geodesic domes.[139]

The C_{60}-fullerene consists of 12 pentagons and 20 hexagons and can be described

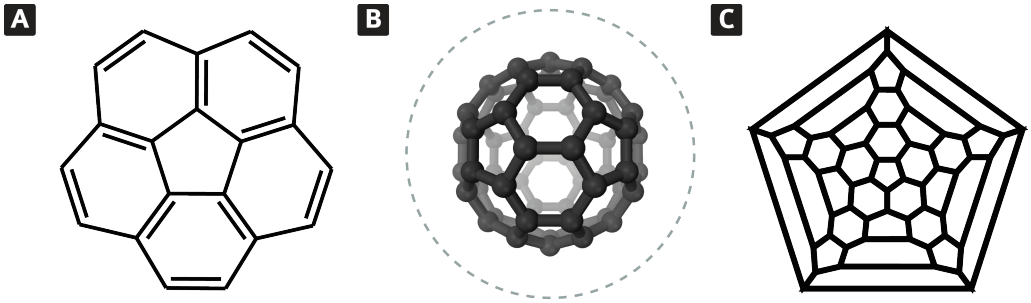

Fig. 7.1.: (A) Corannulene; (B) Three-dimensional representation of C_{60}, the dashed line marks the vdW-radius (Image taken from Wikipedia); (C) Schlegel-diagram showing the connections between the individual carbon atoms.

as a truncated icosaedron (Fig. 7.1 B). The structure can be visualized as well by a Schlegel-diagram (see Fig. 7.1 C), where the connections between the carbon atoms are drawn in a 2D-grid fashion, though their lenghts are not to scale. To resemble its geometric structure in the official name, the IUPAC defined the name of C_{60} as [5,6]-fullerene-C_{60}-I_h in 2002.[141] The numbers 5 and 6 state that only pentagons and hexagons form the cluster, C_{60} defines the number of carbon atoms and I_h describes the icosaedral symmetry of the molecule.

[a] The actual number of carbon allotropes is not quite clear. The most well-known are graphite, fullerenes, carbon nanotubes, cubic and hexagonal diamond. Uncommon allotropes are, e.g., the chaoite[136] or amorphous carbon.[137]

The 30 double bonds present in the molecule can be located either at a bond between a pentagon and a hexagon (referred to as [5,6]-bonds) or between two hexagons (referred to as [6,6]-bonds). Bonding interaction of the frontier orbitals can be found at [6,6], whereas antibonding interaction is found at the [5,6] bonds.[142] This results in a shortening of the [6,6] bonds, since it enables the molecule to decrease its total energy. Thereby, an alternation in bond length is induced, which reduces the aromatic character of the molecule. When adding more electrons to the molecule, for example by intercalation of alkali metals, this alternation in bond length is reduced gradually. With an excess of six electrons (C_{60}^{6-}) equal bond lengths are expected. Further increase of the negative charge results in shorter [5-6]-bonds and longer [6,6]-bonds.[143]

7.2 Pristine C_{60} on Calcite (10.4)

As evident from fig. 7.2 (A), C_{60} molecules form ordered islands on the (10.4) cleavage plane of calcite ($CaCO_3$).[37] Only on a few islands, second-layer occupation is observed. Additionally, a preferential orientation along the [010] substrate direction is observed.

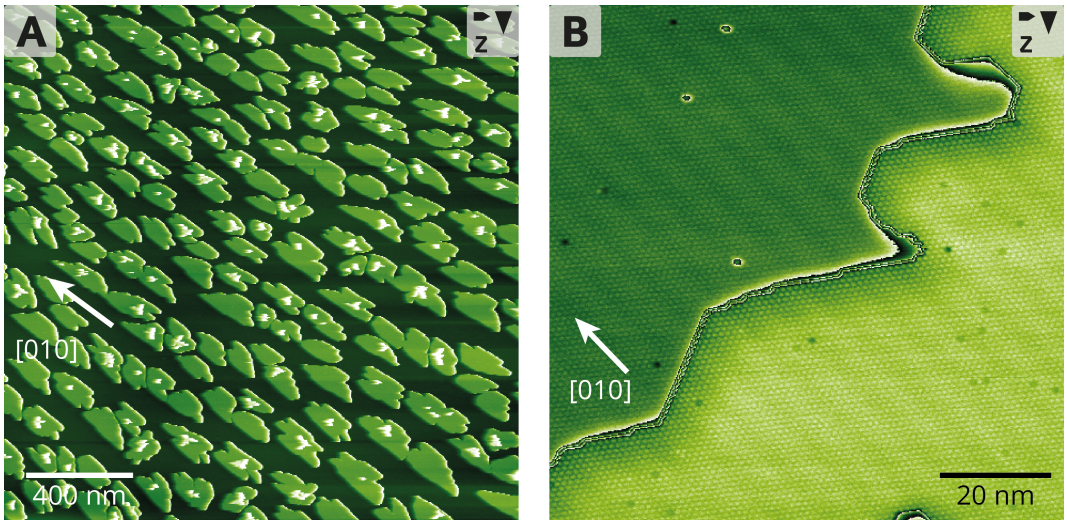

Fig. 7.2.: Overview of pristine C_{60} on the calcite ($10\bar{1}4$) cleavage plane: (A) The islands show a preferential orientation along the [010] substrate direction; (B) the hexagonal arrangement and the moiré pattern are clearly visible on the fist layer (top left) and on the second layer (bottom right).

The apparent height of a single layer is determined to a value of (0.90 ± 0.05) nm. This value has been verified by previous studies from our group[5] and studies of C_{60} deposition on alkali halides.[144] Furthermore, this value lies close to the center-to-center distance of 1 nm in bulk C_{60}.[145]
High resolution images reveal a nearly hexagonal-close packing (see Fig. 7.2 (B)). The distance between adjacent C_{60} molecules was determined to a value of 1.00 ± 0.05 nm.

In addition to that, a moiré pattern with a periodicity of 6.0 ± 0.5 nm is visible. All these values are in excellent agreement to earlier findings.[37]

Based on these findings, our group has proposed an adsorption model for C_{60} on calcite.[5] The hexagonal arrangement of the C_{60} molecules with a neighbour distance of 1.00 ± 0.05 nm is analogue to the arrangement of C_{60} molecules in the (111) facet of bulk face-centered cubic C_{60}. The rectangular unit cell of the calcite (10.4) surface, however, has the dimensions of $0.5 \times 0.81\,\text{nm}^2$ (see lower right corner of Fig. 7.3). Therefore, the distance between adjacent C_{60} molecules fits perfectly into a twofold substrate periodicity alonge the [010] substrate direction. In contrast to this, the neighbour distance of the C_{60} molecules does not match the substrate periodicity of 0.81 nm along the $[\overline{4}21]$ direction. For that reason, a moiré pattern is expected along this direction, which is, indeed, observed in our data. The periodicity of the moiré pattern of 6.0 ± 0.5 nm corresponds to 7.5 repeat units of the unit cell dimension in the $[\overline{4}21]$ direction. Therefore, a (2×15) superstructure is expected, as depicted in Fig. 7.3.

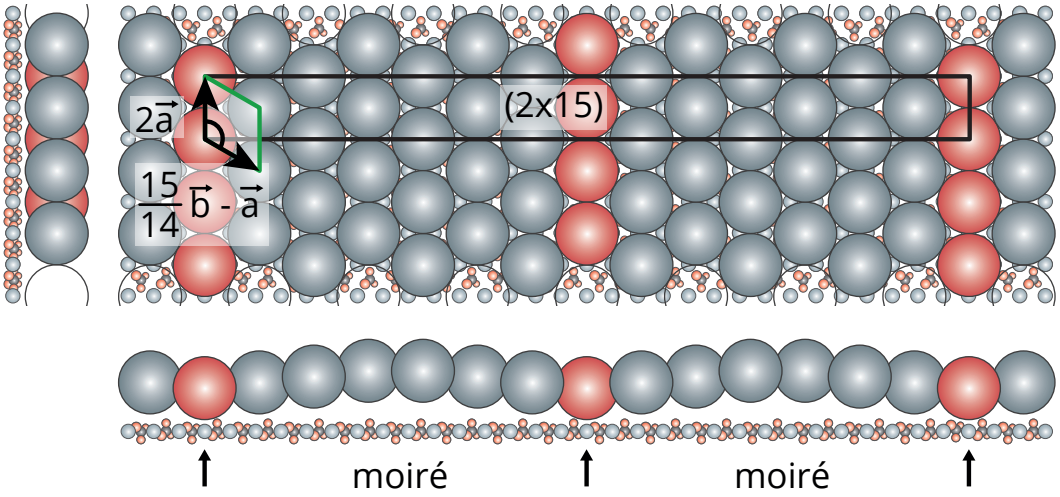

Fig. 7.3.: Adsorption model of pristine C_{60} on calcite.

7.3 Photopolymerization of C_{60} on Calcite (10.4)

Upon irradiation with an appropriate light source, C_{60} fullerenes readily polymerize *via* a [2+2] cycloaddition. This well-known reaction has been widely studied in bulk C_{60}[146,147] and in C_{60} thin films on metal substrates[148,149] and is known to result in a two-dimensional hexapolymer in the bulk. In the following we used a 405 nm laser diode to induce the photopolymerization. Here, we provide a detailed picture explaining how the lattice dimensions of calcite with previously determined values on calcite,[37] alkali halides[144] and in bulk C_{60}.[145] Besides the hexagonal arrangement, a moiré pattern with a periodicity of (6.1 ± 0.5) nm is clearly visible in our AFM images (Fig. 7.4 A) as evident from alternating bright and dark rows

along the [01.0] direction.

When we irradiate C_{60}-covered calcite samples with UV light (405 nm), the coverage and the overall distribution of C_{60} molecules do not notably change. This indicates that the substrate does not heat up significantly during irradiation.[b]

In sharp contrast to the large-scale observations, the molecular-scale details change significantly upon irradiation as shown in Fig. 7.4 B and C. Here, a monolayer of C_{60}

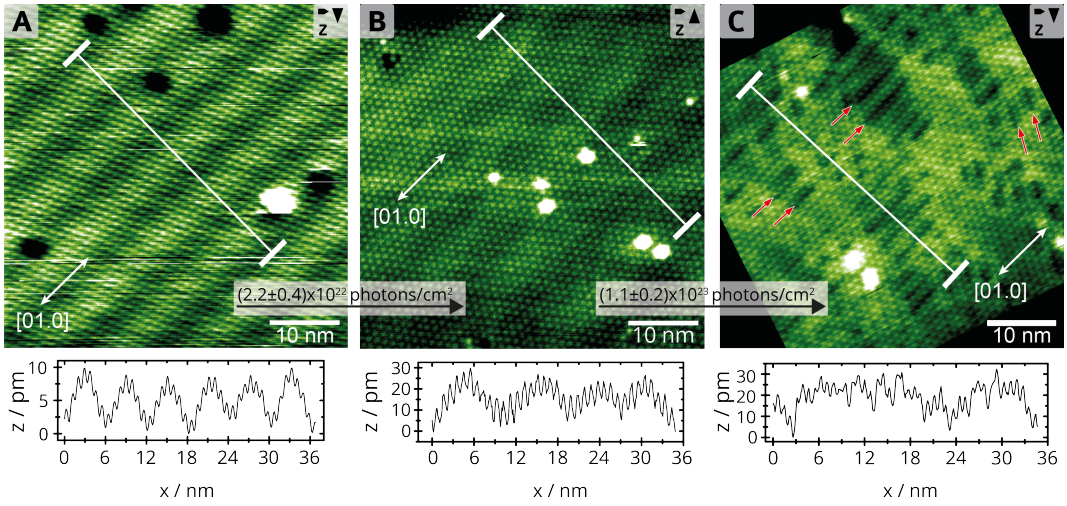

Fig. 7.4.: A monolayer of C_{60} on calcite (10.4) before and after irradiation. Line profiles are extracted at the indicated positions, averaged over 60 pixels: (A) The pristine film shows a moiré pattern. After irradiation, the moiré pattern becomes aperiodic (B) and eventually vanishes (C). Instead, domains separated by dark lines (red arrows) are observed.

was exposed to a total number of $(1.4 \pm 0.2) \cdot 10^{21}$ photons/cm^2 (Fig. 7.4 B). The most prominent change concerns the aperiodic moiré pattern, clearly indicating that the C_{60} islands no longer form a perfect periodic superstructure. This is also evident from the extracted line profile, showing an aperiodic modulation perpendicular to the [01.0] substrate direction. After extended irradiation with a total number of $(4.9 \pm 0.8) \cdot 10^{21}$ photons/cm^2, the molecular arrangement changes even more (Fig. 7.4 C). The moiré pattern vanished completely, clearly indicating a change in the intermolecular distances. Instead of the moiré pattern, dark lines (indicated by the red arrows in Fig. 7.4 C) are identified in the image. These dark lines are gaps between domains of covalently linked C_{60} molecules, as will be corroborated in the following. As can be seen, the domains are predominantly aligned along the [01.0] substrate direction. Evidence for the covalent linkage is given by a detailed analysis of the images. To provide independent evidence for the capability of our setup to induce covalent linkage, both UV-vis spectroscopy as well as mass spectrometry were performed on thick C_{60} films, as presented in appendix A. To elucidate the morphological changes in more detail, we analyze drift-corrected images as shown in Fig. 7.5 A. We observe two distinct features in this image. First, several

[b] In contrast, we can induce molecular dewetting of C_{60} on calcite (10.4) by thermal annealing of the substrate to temperatures above 400 K.

C_{60} molecules appear brighter than the average. Second, some of the C_{60}-C_{60} distances are changed as evident from an analysis of the spatial separation of the molecules (Fig. 7.5 B). Profile 1 reveals the corrugation of four molecules with equidistant intermolecular spacing of (1.08 ± 0.05) nm, in good agreement with a row of individual, unreacted molecules. Interestingly, profile 2 differs significantly from profile 1. In profile 2, the two molecules labelled B and C are considerably closer to each other with a distance of only (0.93 ± 0.05) nm. Accordingly, the distances towards the two neighboring molecules (A and D) are increased to (1.20 ± 0.05) nm and (1.19 ± 0.05) nm. This change in distance strongly suggests a successful covalent linking of the two molecules (B and C), as this distance agrees with previously reported values of polymerized C_{60} in the bulk[147] and in thin-films.[149] The same effect can be seen for a number of C_{60} molecules in Fig. 7.5 B. This finding is particularly obvious when inspecting the group of C_{60} molecules marked with a hexagon. Here, six C_{60} molecules are shifted closer towards the center molecule. To provide further evidence for the change in intermolecular distance, distance histograms before and after irradiation are presented in appendix A, revealing a maximum at a distance of 1.0 nm before reaction. After irradiation, the amount of smaller intermolecular distances at 0.9 nm is notably increased. In Fig. 7.5 (B), molecules which have reacted with more than one neighbor are imaged brighter than others, as demonstrated for molecule B in profile 2 and the center molecule in the hexagon. This leads to an overall heterogeneous appearance of the C_{60} islands after irradiation. We now explain all previous findings with a straightforward model. The

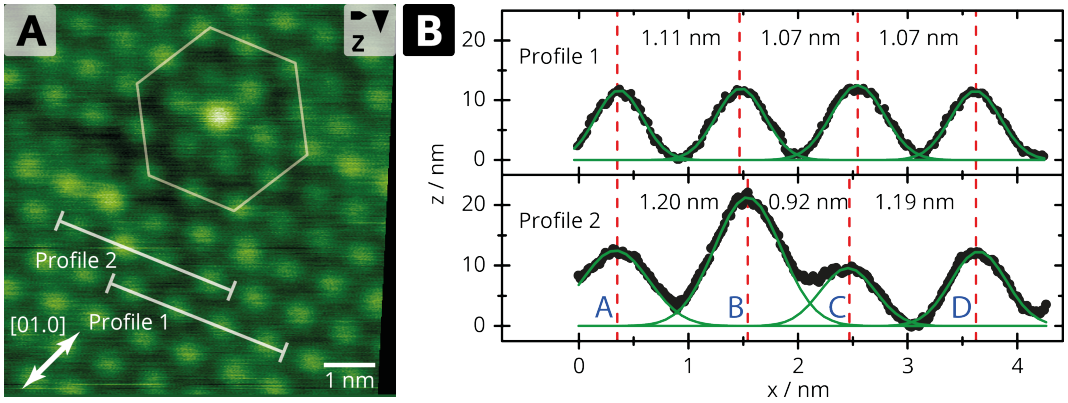

Fig. 7.5.: (a) Image of irradiated C_{60} on calcite (10.4). A change in brightness of individual C_{60} molecules can be observed. (b) Line profiles from (a) revealing a change in some intermolecular distances.

adsorption structure of pristine C_{60} on $CaCO_3$(10.4) is depicted in Fig. 7.3.[35] The measured intermolecular distance of 1 nm excellently matches the two-fold substrate periodicity along the [01.0] direction. In contrast, along the other substrate direction, the C_{60} molecules are out of registry with the surface. The C_{60}-C_{60} row distance in $[42.\bar{1}]$ direction equals $\frac{15}{14}b$, with b being the calcite unit cell vector in $[42.\bar{1}]$ direction, resulting in a (2×15) superstructure. Since every seventh row of C_{60} molecules occupies equivalent adsorption positions on the calcite surface (orange-

colored C_{60} molecules in Fig. 7.3), the observed moiré pattern has a periodicity of $7.5 \cdot b = 6.1\,\text{nm}$[35] which is exactly the periodicity measured in Fig. 7.4 A. We now extend this model to the molecular arrangement after irradiation. As observed in our experiments, irradiation leads to covalent linkage of C_{60} and results in reduced intermolecular distances. We do not expect a covalent linkage along [01.0] due to the excellent match of the intermolecular distance of unreacted C_{60} with the substrate periodicity. Along the other direction, however, the mismatch between substrate periodicity and intermolecular spacing constitutes a driving force for reaction along the $[42.\bar{1}]$ direction. As shown in the scheme in Fig. 7.6, the projected distance of linked molecules along the $[42.\bar{1}]$ direction is reduced from 0.88 nm to 0.81 nm (green and red rhomb, respectively), thus, now excellently matching the periodicity of the underlying substrate. This clearly explains why the moiré pattern vanishes upon irradiation. As indicated in Fig. 7.6, the majority of domains is three-molecules wide along the $[42.\bar{1}]$ direction, which can be understood from the fact that further reaction along the $[42.\bar{1}]$ direction is unlikely due to the increased C_{60}-C_{60} distance in the gaps separating the domains (Fig. 7.5 B). These gaps are visible as dark lines in our images (Fig 7.4 C). This geometrical constraint, thus, guides the reaction along specific substrate directions and results in covalently linked domains with a (2×2) superstructure.

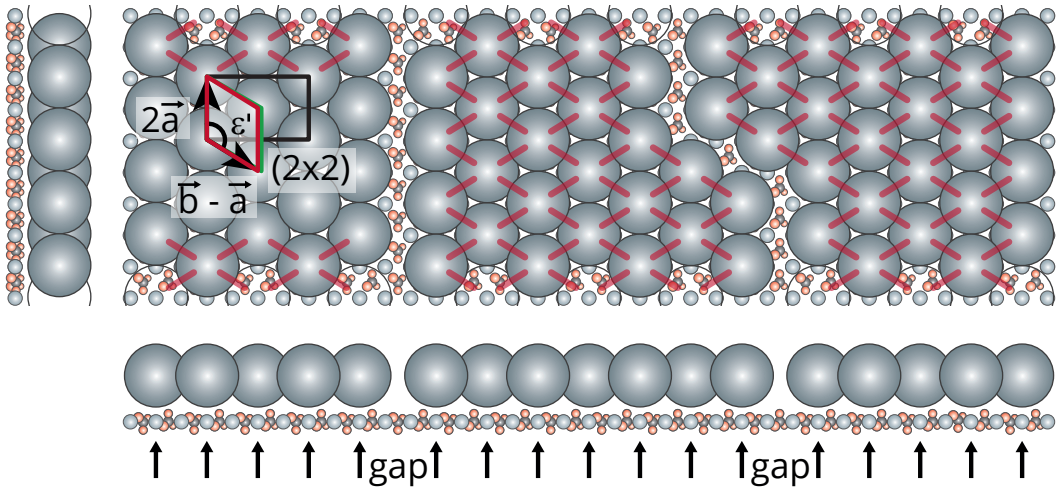

Fig. 7.6.: Model for the formation of covalently linked domains with covalent links marked by red lines. All C_{60} molecules with identical adsorption position are marked by small black (gray) arrows. The green and the red rhomb indicate the C_{60} unit cell before and after irradiation, respectively.

7.4 Statistics on the Polymerization

In order to get a more detailed picture of the directed photopolymerization, we evaluated a number of images quantitatively. Figure 7.7 (A) shows a hexagon of C_{60} on $CaCO_3$ with the main directions indicated by arrows. By counting the

intermolecular distances in several selected images with respect to specific substrate direction, it is evident that the occurrence of C_{60}-C_{60} links along the $[\overline{2}04\overline{5}]$ and the $[2024\overline{5}]$ substrate direction is roughly twice the occurrence of C_{60}-C_{60} links along the [010] direction (see Fig. 7.7 (B)). For an even more detailed examination, we analyzed the occurrence of various oligomers with respect to the direction of the reaction (see Fig. 7.7 (C)). We found that the relative amount of molecules forming a dimer is only 38 % of the total amount of reacted molecules. Furthermore, when taking the individual directions into consideration, 61 % of the dimers are oriented along the [010] direction, 30 % along the $[\overline{2}045]$, and 31 % along the $[2024\overline{5}]$ direction. Thus, the majority of C_{60} dimers are found oriented along the [010] substrate direction, while for the longer oligomers, i.e. trimers - heptamers, the orientation along the $[\overline{2}045]$ and the $[2024\overline{5}]$ is favored.

When comparing the number of oligomerized molecules along the $[\overline{2}045]$ and the

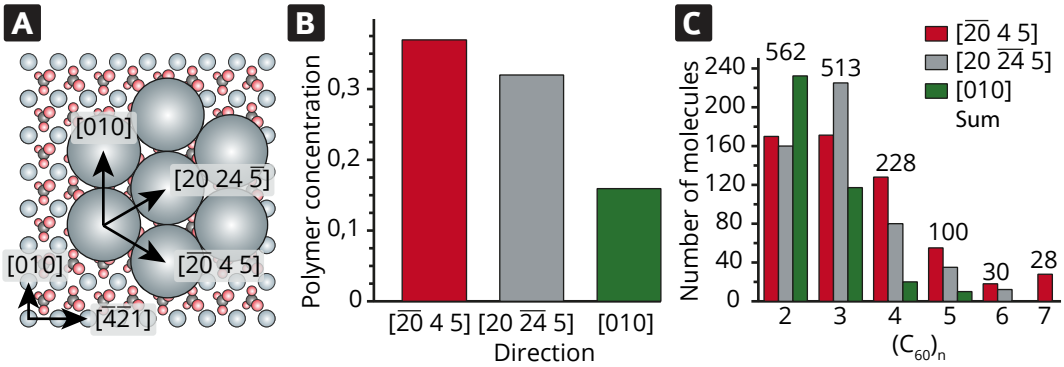

Fig. 7.7.: (A) Model of C_{60} on $CaCO_3$ indicating the directions, with respect to the substrate; (B) Percentage of polymerized C_{60} on calcite (10.4) with respect to the direction; (C) Total number of molecules that reacted along a certain direction.

$[2024\overline{5}]$ direction in Fig. 7.7 (C), it is clearly visible that the majority of molecules form trimers and only smaller fractions are forming dimers and tetramers. Higher oligomers are only scarcely observed. This obersvation can be readily explained when comparing the C_{60}-C_{60} distances for the oligomers found on the surface. For that we use a simple force-field optimization[c] of the respective oligomer and compare them to the periodicity of the $[42\overline{1}]$ substrate direction, with $l = 0.81$ nm. As elucidated earlier, the reaction is driven by the minimization of the lattice mismatch along the $[42\overline{1}]$ direction. As evident from Tab. 7.1, the deviation from the substrate periodicity exhibits a minimum for C_{60} trimers with $\Delta d = 1.08\%$. For higher oligomers, i.e. trimers, tetramers, etc., the deviation increases again, because now the C_{60}-C_{60} distance becomes too short. Thus, the mismatch between the two lattices promotes the reaction, but only until a C_{60} trimer is formed. For higher oligomers, the increase in deviation hampers the reaction. Additionally, longer distances between the molecules have to be overcome. However, for all oligomers, the deviation is significantly less than for pristine C_{60}. We have to stress that, given

[c] *Universal Force Field* within the software *Avogadro*

the simple approach of the calculation, the absolute numbers may exhibit a certain error. However, a definite trend is evident.

Tab. 7.1.: Averaged intermolecular distances of C_{60} and C_{60} oligomers; $d\|[42\bar{1}]$ represents the C_{60} distance projected onto the $[42\bar{1}]$ substrate direction.

$(C_{60})_n$	$d(C_{60} - C_{60}, avg.)$ / nm	$d\|[42\bar{1}]$ / nm	Δd/ %
1	1,000	0.866	6.47
2	0.915	0.792	2.21
3	0.925	0.801	1.08
4	0.909	0.787	2.91
5	0.908	0.786	3.05
6	0.916	0.793	2.13
7	0.925	0.801	1.16

7.5 Conclusion

In summary, we demonstrate a substrate-guided photochemical reaction on a bulk insulator. The success of the covalent linkage is evident from a shortening of the intermolecular distances, which is clearly expressed by the disappearance of the moiré pattern. Furthermore, UV-vis and mass spectroscopy measurements carried out on thick films demonstrate the ability of our setup for initiating the photo-induced reaction and, thus, corroborate this assignment. The irradiation of C_{60} results in well-oriented covalently linked domains. Most importantly, the orientation of these domains is dictated by the lattice dimensions of the underlying calcite substrate. This is further corroborated by a quantitative analysis, showing a strong dependence of the polymerization direction on the oligomer length. The formation of domains consisting of three rows of C_{60} is readily explained by minimizing the lattice mismatch. The deliberate steering of the direction of a chemical reaction using the lattic mismatch is expected to constitute a general design principle for on-surface synthesis. Therefore, our work provides a strategy for controlled fabrication of oriented, covalent networks on bulk insulators.

8

Caesium-doped C_{60}

Application in molecular electronics will require strategies for the fabrication of stable fullerene structures on a supporting surface. On metals, which typically possess rather large surface energies, C_{60} has been shown to form stable wetting layers.[37] However, metal substrates are not suited when having electronic applications in mind. Consequently, for decoupling the electronic structure of the molecular device from the support, electrical insulating substrates have to be used. Unfortunately, most insulators exhibit a rather low surface energy and, thus, C_{60} tends to dewet from these surface already at comparatively low temperatures.[37] On calcite, for example, C_{60} starts to dewet at around 400 K.[150] This dewetting tendency severely hampers the applicability of self-assembled structures on bulk insulators, explaining the pressing need for strategies to enhance the molecule-surface interaction in these systems.[33] Several mechanisms have already been discussed, such as increasing the molecule-substrate interaction by a precise matching between molecular functional groups and the surface lattice. Moreover, deprotonation of the molecular species, or increasing the number of functional groups provides a straightforward strategy for increasing the molecule-surface interaction.[33] For pure C_{60}, however, these approaches are not applicable, due to the lack of functional groups. In this system, the molecule-substrate interaction can be enhanced by enlarging the ionic character of the system, i.e., by doping with electrons. This approach has proven to greatly enhance the stability of self-assembled C_{60} layers on hydrogen-terminated diamond[151] and on highly oriented pyrolytic graphite (HOPG).[152] On hydrogen-terminated diamond, this is accomplished by a transfer of electrons from the substrate into the molecular islands, resulting in stable wetting layers. On HOPG, the doping of C_{60} with elementary caesium has been shown to result in a substantially higher desorption temperature. While pristine C_{60} desorbs from HOPG at 560 K, increasing the doping with Cs gradually shifts the peak to 700 K, where Cs_xC_{60} ($x < 4$) clusters desorb. Further doping with Cs allows for the formation of Cs_xC_{60} ($x > 4$) clusters, which do not desorb from the surface up to a temperature of 880 K. This can be explained by a transfer of electrons from the caesium to the C_{60}. Comparing the electron affinity of C_{60} ($E_A(C_{60}) = -3.98\,eV$)[153] with the ionization energy of Cs ($E_I(Cs) = +3.89\,eV$)[154] shows why the electron transfer is energetically favored.

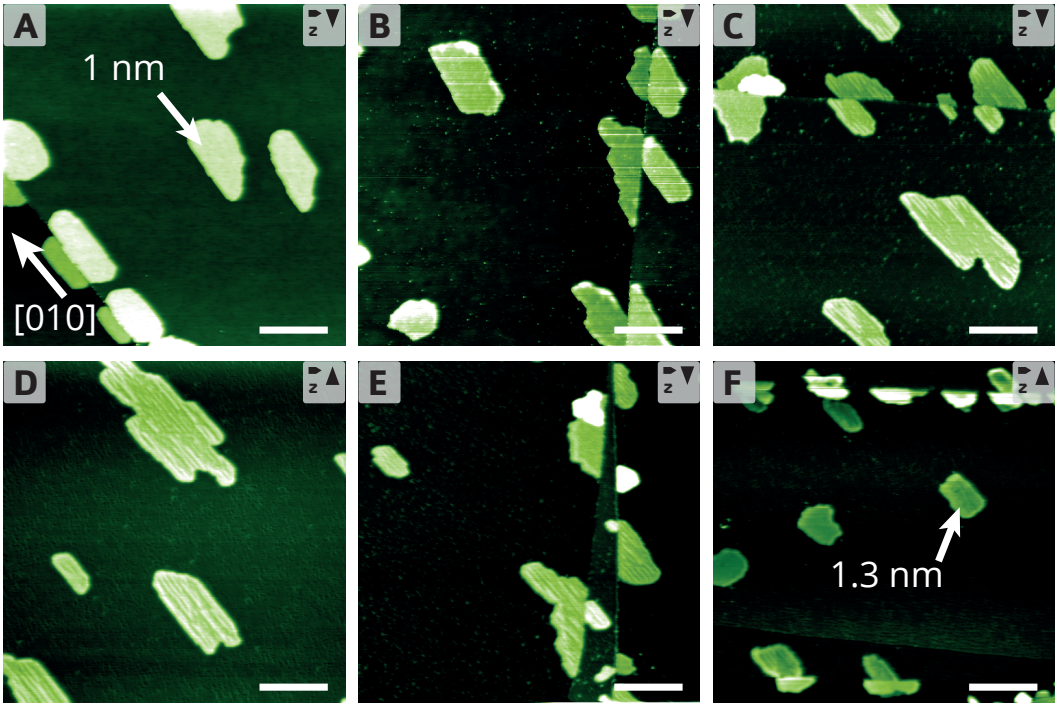

Fig. 8.1.: (a) Pristine C_{60} islands on $CaCO_3$, coverage $\Theta = 0.21$ ML; Stepwise doping with (b) 0.05 ML, (c) 0.15 ML, (d) 0.20 ML, (e) 0.30 ML, (f) 0.35 ML of Cs. The scale bar corresponds to 200 nm

8.1 Stepwise Doping

In order to observe the change in island appearance upon deposition of Cs onto C_{60}, we dosed Cs in a step-by-step fashion onto pre-deposited C_{60} monolayer islands. Fig. 8.1 shows the trend when gradually increasing the amount of Cs by 0.05 ML per step. The ratio of C_{60} and Cs can be easily calculated, when taking into account the vdW radii of C_{60} and Cs. Since 1 ML Cs consists of four times more particles than 1 ML C_{60}, after the deposition of 0.21 ML C_{60} and 0.05 ML Cs, the molar ratio is $r \approx 1:1$. For the case of pristine C_{60} (Fig. 8.1 A), the well-known apparent island height of 1 nm is observed,[37,150] which is in perfect agreement with the van-der-Waals radius in bulk C_{60}.[155] After dosing an equivalent of 0.05 ML Cs, a faint halo can be observed on parts of the fringe of the C_{60} islands (see Fig. 8.1 B). Additionally, bright lines on top of the islands along the fast scan direction can be observed. With increasing Cs-dose the whole fringe of the C_{60} islands becomes equally bright (C) and stripes reaching from the fringe to the interior of the island can be seen (D). These stripes are oriented along the [010] substrate direction, which is the same direction as the moiré pattern observed for pristine C_{60}. Further doping first elongates and then broadens the observed stripes (Fig. 8.1 D & E), until the whole island exhibits a uniform height of 1.32 nm (see Fig. 8.1 F). The increased height of 320 pm is in good agreement with a cation radius of Cs^+ of $r = 167\,pm$.[154] When measuring the imaging height of apparent double layers of C_{60}, their height of 2.3 nm corresponds

well with the calculated value of two layers of C_{60} and one layer of Cs.

Fig. 8.2 A depicts a closer look onto the stripes, after the deposition of 0.20 ML

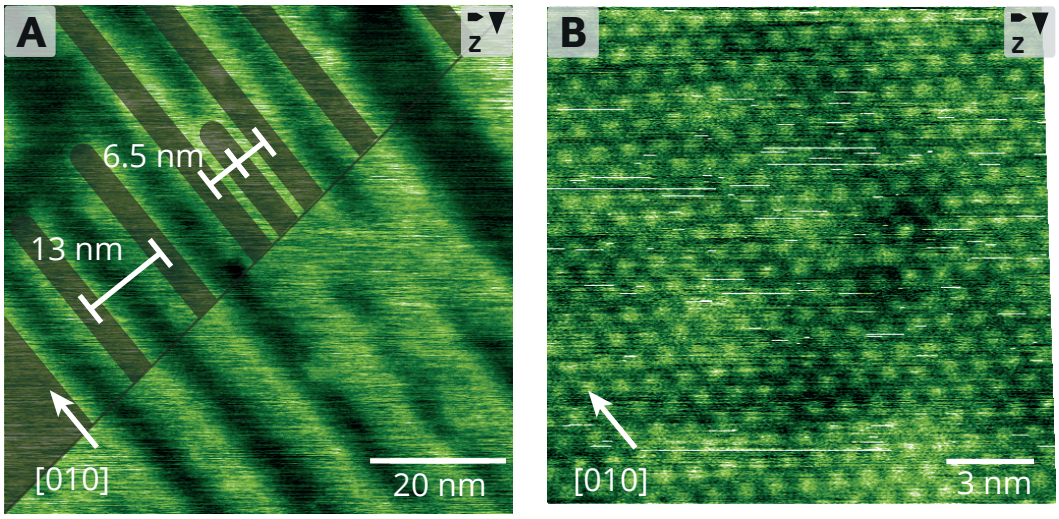

Fig. 8.2.: Closeup of 0.20 ML of Cs on 0.21 ML C_{60}: (a) Stripes with a distance of 13 nm and 6.5 nm can be observed; (b) Increasing tip-sample interaction reveals a heterogeneous, hexagonal C_{60} pattern

of Cs onto monolayer islands of C_{60}, corresponding to a nominal composition of Cs_4C_{60}. These stripes exhibit a width of circa 5.5 nm and a repeat distance between two neighbouring stripes of 13 nm and 6.5 nm, respectively. The stripe distance corresponds very well with the periodicity of the C_{60} moiré pattern of 6.5 nm (see Chap. 7). Additionally, the stripes exhibit no internal periodicity, except a noisy pattern along the fast scan direction. Even upon cooling the sample to 100 K, no periodicity in the stripes can be observed. However, when increasing the detuning setpoint, and, thus, enlarging the force between tip and sample, the hexagonal structure of C_{60} can be observed (see Fig. 8.2 B).

When comparing the periodicity of the observed stripes with the periodicities of the underlying C_{60}, it can be seen that they are always whole-number multiples of the moiré pattern periodicity. Thus, the stripes are most likely to be related to the electronic modulation of the moiré pattern.[37]

8.2 Annealing Behaviour

After these initial observations, we investigated the thermal behavior of the islands. At 300 K (Fig. 8.3 (A)) monolayer islands are observed, exhibiting the previously discussed bright fringe and stripes on top of the C_{60} islands. After a first annealing step at 410 K for 1 h (Fig. 8.3 (B)), the onset of disintegration of the islands can be observed. This is easily visible from the formation of holes in the interior of the islands. Additionally, some second layer occupation is observed. At first glance, the

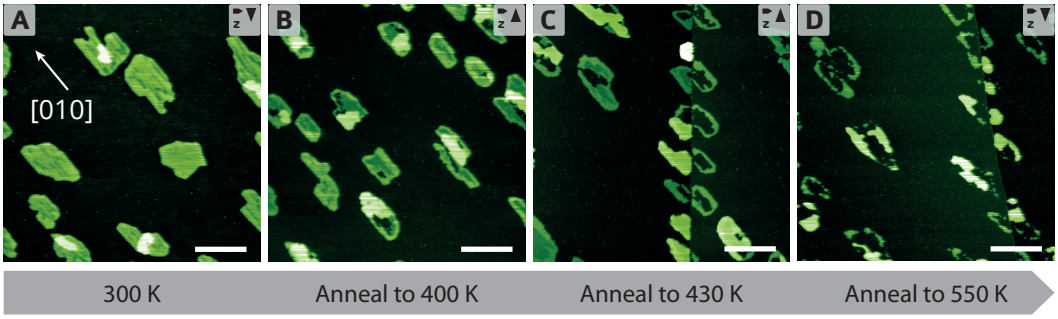

Fig. 8.3.: Dewetting behaviour of Cs doped C_{60} islands upon increasing annealing temperature. First the interior of the islands start to dewet to form double layers, until only the island borders are remaining. The scale bar corresponds to 200 nm.

dewetting from the interior is contradictory to the dewetting behaviour of pristine C_{60}, which starts to dewet from the borders of the island. This situation becomes even more pronounced at higher annealing temperatures. Upon further heating to 430 K for 1 h, the dewetting from the interior of the islands continues, yet the borders of the islands are still clearly visible (Fig. 8.3 (C)). Increasing the temperature to 550 K leaves only the borders of the islands on the surface. However, the borders do not form a closed ring anymore, but a discontinuous line (Fig. 8.3 (D)). From these observations we can conclude that the interaction with the substrate is significantly increased when doping C_{60} with Cs, most notably at the island fringes.
The observed effects are readily understandable by the energetically favoured electron transfer from the Cs atoms to the C_{60} islands. This follows immediately when comparing the electron affinity of C_{60} ($E_A(C_{60}) = -3.98\,eV$)[153] with the ionization energy of Cs ($E_I(Cs) = +3.89\,eV$).[154]

8.3 KPFM Contrast

To further corroborate the above shown results, KPFM appears as an obvious method, since it bears the potential for imaging of local charge.[20] However, the theory behind KPFM is only well understood for the simplified situation of the surface and the tip both being conductive. Our system, in contrast, consists of a bulk insulator and a semiconducting tip, with no information on the microscopic structure. For such a system, a comprehensive model for KPFM contrast formation is still lacking. Therefore, even a relative statement of a charge accumulation in the molecular islands with respect to the surface cannot be made in our case.
Despite this, we performed simultaneous KPFM on Cs-doped C_{60} islands. Note that all values are given with respect to the calcite surface. Figure 8.4 shows the simultaneously recorded topology (A) and KPFM (B) images. Several striking observations are revealed. When comparing the island in Fig. 8.4 (A) & (B), it can be seen that all larger parts that are imaged bright in the topography exhibit

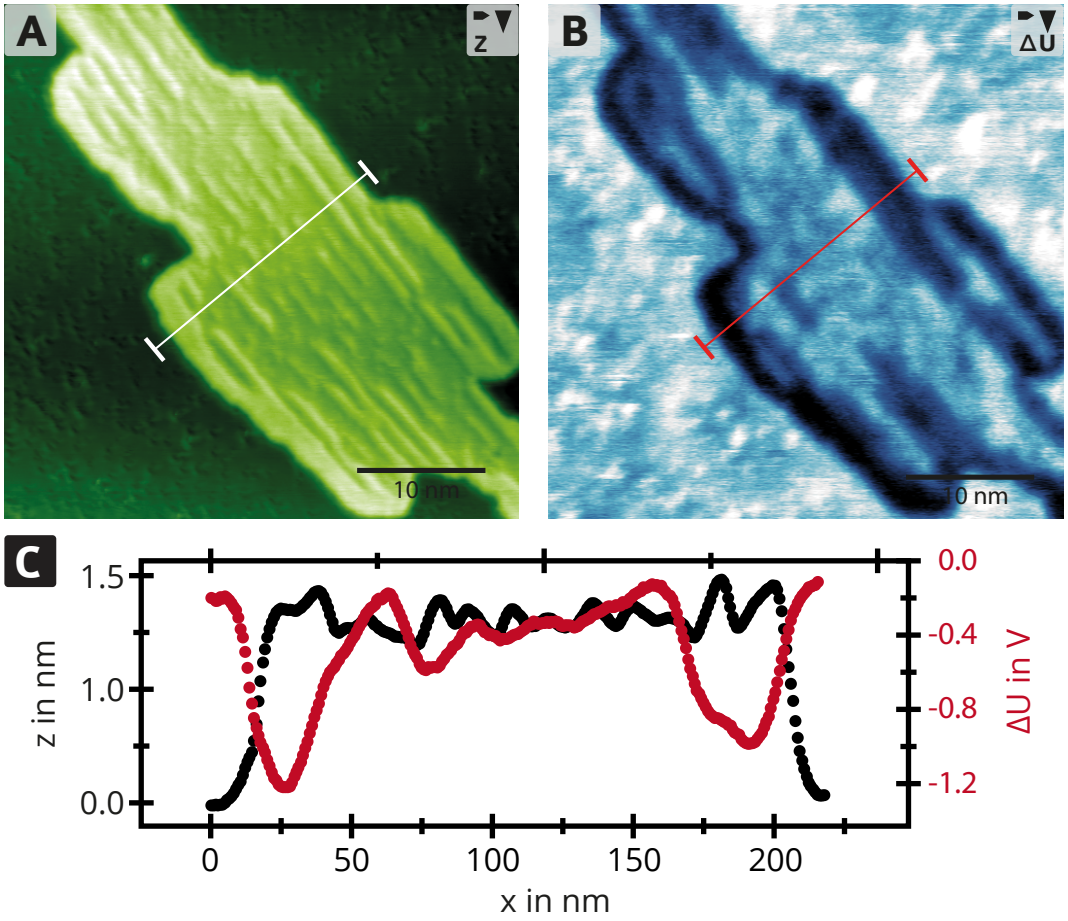

Fig. 8.4.: Topography (A) and KPFM image (B) of a C_{60} islands doped with Cs; (C) Extracted and averaged line profiles from the indicated positions in A and B.

an apparent negative signal in KPFM with respect to the bare substrate. This negative shift is particularly pronounced at the island fringes, as can be seen from the extracted line profiles shown in Fig. 8.4 (C). Around the island, several molecular clusters can be observed, which appear with a positive KPFM value.

As mentioned, the interpretation of these results requires further insights in KPFM contrast formation, which are not available at present. If we assume the tip being conductive, the KPFM results would agree with the above drawn picture of an electron transfer from the Cs into the C_{60} islands. In this case, the localization of negative charges at the fringes would be understandable when considering the mobility of charges in C_{60} monolayers:[156] The charges accumulate at the perimeter of the C_{60} island to maximize the distance between the charges. Thus, in light of the results from the annealing experiments, interpreting the KPFM results with the simplified model of a conductive tip appears reasonable.

8.4 Conclusions

In summary, we have shown that upon doping monolayer islands of C_{60} with Cs, the interaction with the substrate is significantly increased. This is evident from a rise in desorption temperature to 650 K, in sharp contrast to pristine C_{60} on $CaCO_3$. This result is readily explained by an electron transfer from the Cs atoms into the C_{60} islands. The presented stabilisation mechanism is not specific to calcite as substrate. This offers the option to explore this route as a universal mechanism for enhancing the molecule-surface interaction on various substrate surfaces. Moreover, in contrast to charge-transfer stabilization concepts that have been presented before, Cs doping provides the potential to fine-tune the interaction strength by varying the Cs concentration.

9 Summary

In conclusion, this thesis presents a comprehensive study of molecular self-assembly and the deliberate modification of self-assembled structures. State-of-the art non-contact atomic force microscopy operated in ultra-high vacuum provides a most powerful tool for investigating molecular self-assembly and on-surface synthesis at the single molecule level.

The self-assembly of molecules is based on a very delicate balance of the involved interactions. On the one hand the molecules have to diffuse readily on the surface, while on the other they have to interact strongly enough to form stable molecular islands. This is exemplarily shown for two molecules from the class of perylenes presented in chapter 6. PTCDA and its fourfold chlorinated derivative TCPTCDA show a strikingly divergent self-assembly behaviour. PTCDA is diffusing readily on the calcite surface, not showing any tendency to self-assemble into islands. Nevertheless, PTCDA is found to orient itself towards a specific substrate direction. TCPTCDA, however, adopts a hereunto perpendicular adsorption geometry. Most importantly, it forms stable islands, within which two mirror-symmetrical domains are observed. This substantial difference is attributed to the increased interaction stemming from the negatively polarized chlorine substituents and a decisive change in the dimensions of the molecule. This study demonstrates that a rational design of the involved molecular building blocks constitutes a powerful tool for controlling the resulting structure formation by adjusting the delicate interaction balance.

In chapter 7, I present the first example for a photochemically initiated on-surface reaction on a bulk insulator. The success of the reaction is directly evident from a shortening of the C_{60}-C_{60} distances. Additionally, domains of covalently linked C_{60} molecules are observed. The orientation of these domains is understood by considering the dimensions of the underlying substrate, which favours the reaction along specific substrate directions. This is evident from a qualitative investigation of high-resolution AFM images. Moreover, this interpretation is significantly corroborated by a quantitative analysis proving a preferred reaction along the substrate directions not parallel to [010]. Minimizing the lattice mismatch between the molecular structure and the underlying calcite lattice is revealed to constitute the driving force for the observed directionality of the reaction. This study clearly demonstrates the option to steer the direction of the on-surface reaction by the right choice of underlying substrate.

The controlled enhancement of the molecule-substrate interaction is presented in chapter 8. Upon doping monolayer islands of C_{60} by controlled deposition of Cs atoms, the interaction with the substrate is significantly increased. This is evident from a rise in desorption temperature, in sharp contrast to pristine C_{60} on $CaCO_3$. This result is readily explained by the transfer of electrons from the Cs atoms into the C_{60} islands. The presented stabilisation mechanism is not restricted to calcite as substrate. Therefore, it offers the option to employ this concept as a general mechanism for a controlled enhancement of the molecule-surface interaction independent of the substrate surfaces. Moreover, controlling the amount of Cs deposited onto the surface provides the potential to fine-tune the interaction strength.

In summary, the results of this thesis demonstrate the importance of rational approaches to create functional structures on surfaces. The presented strategies for steering the process of molecular self-assembly, controlling on-surface synthesis and enhancement of the molecule-substrate interaction, will contribute to a further advancement in the development of complex structures on surfaces at the molecular scale.

Bibliography

[1] K. Goser, P. Glösekötter, J. Dienstuhl, *Nanoelectronics and Nanosystems*, Springer, Berlin, **2004**.

[2] M. Kaku, *Physics of the Future*, Knopf Doubleday Publishing Group, **2011**.

[3] G. M. Whitesides, J. P. Mathias, C. T. Seto, *Science* **1991**, *254*, 1312.

[4] G. Franc, A. Gourdon, *Phys. Chem. Chem. Phys.* **2011**, *13*, 14283.

[5] P. Rahe, PhD Thesis, Johannes Gutenberg-Universität Mainz, **2011**.

[6] M. Xiao, *Opt. Commun.* **1996**, *132*, 403.

[7] T. L. Makarova et al., *J. Appl. Phys.* **2011**, *109*, 083941.

[8] R. Young, J. Ward, F. Scire, *Rev. Sci. Instrum.* **1972**, *43*, 999.

[9] G. Binnig, H. Rohrer, C. Gerber, E. Weibel, *Phys. Rev. Lett.* **1982**, *49*, 57.

[10] G. Binnig, C. F. Quate, *Phys. Rev. Lett.* **1986**, *56*, 930.

[11] T. R. Albrecht, *J. Vac. Sci. Technol. A* **1990**, *8*, 3386.

[12] F. J. Giessibl, *Rev. Mod. Phys.* **2003**, *75*, 949.

[13] T. R. Albrecht, P. Grutter, D Horne, D Rugar, *J. Appl. Phys.* **1991**, *69*, 668.

[14] H. Ito, S. Nagano, M. Kumagai, M. Kajita, Y. Hando, *Appl. Phys. Express* **2013**, *6*, 102202.

[15] V. F. Kroupa, *Phase Lock Loops and Frequency Synthesis*, John Wiley & Sons, Ltd, Chichester, UK, **2003**.

[16] J. E. Lennard-Jones, *Proc. Phys. Soc.* **1931**, *43*, 461.

[17] D. Upper, *J. Appl. Behav. Anal.* **1974**, *7*, 497.

[18] L. Kelvin, *Philos. Mag. Ser. 5* **1898**, *46*, 82.

[19] W. a. Zisman, *Rev. Sci. Instrum.* **1932**, *3*, 367.

[20] M. Nonnenmacher, M. P. O'Boyle, H. K. Wickramasinghe, *Appl. Phys. Lett.* **1991**, *58*, 2921.

[21] J. Neff, P. Rahe, *Phys. Rev. B* **2015**, in press.

[22] M. Kittelmann, PhD Thesis, Johannes Gutenberg-Universität Mainz, **2013**.

[23] *Carbonates: Mineralogy and Chemistry*, (Ed.: R. J. Reeder), Mineralogical Society of America, Chantilly, VA 20151-1110 United States, **1983**, p. 399.

[24] J. D. Currey, *J. Exp. Biol.* **1999**, *202*, 3285.

[25] H. Cölfen, *Curr. Opin. Colloid Interface Sci.* **2003**, *8*, 23.

[26] M. E. Tucker, V. P. Wright, *Carbonate Sedimentology*, Wiley-Blackwell, **2009**, p. 496.

[27] R. N. Smartt, W. H. Steel, *J. Opt. Soc. Am.* **1959**, *49*, 710.

[28] B. Zhang, Y. Luo, X. Liu, G. Barbastathis, *Phys. Rev. Lett.* **2011**, *106*, 033901.

[29] A. Le Floch et al., *Proc. R. Soc. A Math. Phys. Eng. Sci.* **2013**, *469*, 20120651.

[30] P. W. Mirwald, *Phys. Chem. Miner.* **1979**, *4*, 291.

[31] J. W. Anthony, R. A. Bideaux, K. W. Bladh in, Mineralogical Society of America, Chantilly, VA, US, 5th ed., **2003**, Chapter Calcite.

[32] D. Baer, D. L. Blanchard, *Appl. Surf. Sci.* **1993**, *72*, 295.

[33] P. Rahe et al., *Adv. Mater.* **2013**, *25*, 3948.

[34] M. Kittelmann et al., *J. Phys. Chem. C* **2013**, *117*, 23868.

[35] P. Rahe et al., *J. Phys. Chem. C* **2010**, *114*, 1547.

[36] C. M. Hauke et al., *J. Phys. Chem. C* **2012**, *116*, 4637.

[37] P. Rahe, R. Lindner, M. Kittelmann, M. Nimmrich, A. Kühnle, *Phys. Chem. Chem. Phys.* **2012**, *14*, 6544.

[38] S. L. S. Stipp, C. M. Eggleston, B. S. Nielsen, *Geochim. Cosmochim. Acta* **1994**, *58*, 3023.

[39] A. L. Rachlin, G. S. Henderson, M. C. Goh, *Am. Mineral.* **1992**, *77*, 904.

[40] A. Gourdon, *Angew. Chem. Int. Ed.* **2008**, *47*, 6950.

[41] A. Kühnle, *Curr. Opin. Colloid Interface Sci.* **2009**, *14*, 157.

[42] F. Ullmann, *Justus Liebig's Ann. der Chemie* **1904**, *332*, 38.

[43] L. Grill et al., *Nat. Nanotechnol.* **2007**, *2*, 687.

[44] S. Hla, L Bartels, G Meyer, K. Rieder, *Phys. Rev. Lett.* **2000**, *85*, 2777.

[45] Y Okawa, M Aono, *Nature* **2001**, *409*, 683.

[46] J. A. Lipton-Duffin, O Ivasenko, D. F. Perepichka, F Rosei, *Small* **2009**, *5*, 592.

[47] Q. Fan et al., *Angew. Chem. Int. Ed.* **2013**, *52*, 4668.

[48] J. A. Lipton-Duffin et al., *Proc. Natl. Acad. Sci. U. S. A.* **2010**, *107*, 11200.

[49] R. Gutzler et al., *Chem. Commun.* **2009**, 4456.

[50] A. Wiengarten et al., *J. Am. Chem. Soc.* **2014**, *136*, 9346.

[51] M. In't Veld, P. Iavicoli, S. Haq, D. B. Amabilino, R. Raval, *Chem. Commun.* **2008**, 1536.

[52] D. Zhong et al., *Science* **2011**, *334*, 213.

[53] K. T. Rim et al., *Angew. Chem. Int. Ed.* **2007**, *46*, 7891.

[54] G. Otero et al., *Nature* **2008**, *454*, 865.

[55] K. Amsharov et al., *Angew. Chem. Int. Ed.* **2010**, *49*, 9392.

[56] H.-Y. Y. Gao et al., *J. Phys. Chem. C* **2014**, *118*, 6272.

[57] J. E. Mc Murry, M. P. Fleming, *J. Am. Chem. Soc.* **1974**, *96*, 4708.

[58] O. Díaz Arado et al., *ACS Nano* **2013**, *7*, 8509.

[59] M. Matena, T. Riehm, M. Stöhr, T. A. Jung, L. H. Gade, *Angew. Chem. Int. Ed.* **2008**, *47*, 2414.

[60] M. Matena et al., *Chemistry* **2010**, *16*, 2079.

[61] D. G. de Oteyza et al., *Science* **2013**, *340*, 1434.

[62] R. R. Jones, R. G. Bergman, *J. Am. Chem. Soc.* **1972**, *94*, 660.

[63] Q. Sun et al., *J. Am. Chem. Soc.* **2013**, *135*, 8448.

[64] J. Liu, P. Ruffieux, X. Feng, K. Müllen, R. Fasel, *Chem. Commun.* **2014**, 11200.

[65] C. Glaser, *Berichte der Dtsch. Chem. Gesellschaft* **1869**, *2*, 422.

[66] Y.-Q. Zhang et al., *Nat. Commun.* **2012**, *3*, 1286.

[67] J. Eichhorn, W. M. Heckl, M. Lackinger, *Chem. Commun.* **2013**, *49*, 2900.

[68] B. Cirera et al., *ChemCatChem* **2013**, *5*, 3281.

[69] B. Cirera et al., *Nano Lett.* **2014**, *14*, 1891.

[70] L Lafferentz et al., *Nat. Chem.* **2012**, *4*, 215.

[71] R Scholl, C. Seer, R Weitzenböck, *Berichte der Dtsch. Chem. Gesellschaft* **1910**, *43*, 2202.

[72] J. Cai et al., *Nature* **2010**, *466*, 470.

[73] Y. P. Lin et al., *J. Phys. Chem. C* **2013**, *117*, 9895.

[74] S. Weigelt et al., *Angew. Chem. Int. Ed.* **2007**, *46*, 9227.

[75] S. Weigelt et al., *Angew. Chem. Int. Ed.* **2008**, *47*, 4406.

[76] S. Weigelt et al., *ACS Nano* **2008**, *2*, 651.

[77] S. Weigelt et al., *J. Am. Chem. Soc.* **2008**, *130*, 5388.

[78] M. Treier, R. Fasel, N. R. Champness, S. Argent, N. V. Richardson, *Phys. Chem. Chem. Phys.* **2009**, *11*, 1209.

[79] M. Treier, N. V. Richardson, R. Fasel, *J. Am. Chem. Soc.* **2008**, *130*, 14054.

[80] N. A. A. Zwaneveld et al., *J. Am. Chem. Soc.* **2008**, *130*, 6678.

[81] R. Coratger, B. Calmettes, M. Abel, L. Porte, *Surf. Sci.* **2011**, *605*, 831.

[82] C. H. Schmitz, J. Ikonomov, M. Sokolowski, *J. Phys. Chem. C* **2009**, *113*, 11984.

[83] C. H. Schmitz, J. Ikonomov, M. Sokolowski, *J. Phys. Chem. C* **2011**, *115*, 7270.

[84] C. Schmitz, M. Schmid, *J. Phys. Chem. C* **2011**, 18186.

[85] S. Jensen, H. Früchtl, C. J. Baddeley, *J. Am. Chem. Soc.* **2009**, *131*, 16706.

[86] F. Bebensee et al., *J. Am. Chem. Soc.* **2013**, *135*, 2136.

[87] R. Huisgen, *Proc. Chem. Soc.* **1961**, *17*, 357.

[88] H. C. Kolb, M. G. Finn, K. B. Sharpless, *Angew. Chem. Int. Ed.* **2001**, *40*, 2004.

[89] P. Fesser et al., *Chemistry* **2011**, *17*, 5246.

[90] M. Xi, B. E. Bent, *Surf. Sci. Lett.* **1992**, *278*, A69.

[91] M. Di Giovannantonio et al., *ACS Nano* **2013**, *7*, 8190.

[92] M. Koch, M. Gille, A. Viertel, S. Hecht, L. Grill, *Surf. Sci.* **2014**, *627*, 70.

[93] R. Gutzler et al., *Nanoscale* **2014**, *6*, 2660.

[94] M. Bieri et al., *Chem. Commun.* **2009**, 6919.

[95] M. Bieri et al., *Chem. Commun.* **2011**, *47*, 10239.

[96] S. Schlögl, T. Sirtl, J. Eichhorn, W. M. Heckl, M. Lackinger, *Chem. Commun.* **2011**, *47*, 12355.

[97] J. Eichhorn et al., *ACS Nano* **2014**, 7880.

[98] F. Schlütter et al., *J. Am. Chem. Soc.* **2013**, *135*, 4550.

[99] L. Smykalla, P. Shukrynau, M. Korb, H. Lang, M. Hietschold, *Nanoscale* **2015**, *just accep*, DOI 10.1039/C4NR06371F.

[100] T. Lin, G. Kuang, X. S. Shang, P. N. Liu, N. Lin, *Chem. Commun.* **2014**, *50*, 15327.

[101] L. Massimi et al., *J. Phys. Chem. C* **2015**, 2427.

[102] S. Schlögl, W. M. Heckl, M. Lackinger, *Surf. Sci.* **2012**, *606*, 999.

[103] M. Kittelmann et al., *ACS Nano* **2011**, *5*, 8420.

[104] M. Kittelmann, M. Nimmrich, R. Lindner, A. Gourdon, A. Kühnle, *ACS Nano* **2013**, *7*, 5614.

[105] C. Bombis et al., *Angew. Chem. Int. Ed.* **2009**, *48*, 9966.

[106] C. Morchutt, J. Björk, S. Krotzky, R. Gutzler, K. Kern, *Chem. Commun.* **2015**, *51*, 2440.

[107] D Sloan, Y. Sun, H Ihm, J. M. White, *J. Phys. Chem. B* **1998**, *102*, 6825.

[108] C.-A. Palma et al., *J. Am. Chem. Soc.* **2014**, *136*, 4651.

[109] H.-Y. Y. Gao et al., *J. Phys. Chem. C* **2013**, *117*, 18595.

[110] H.-Y. Y. Gao et al., *Angew. Chem. Int. Ed.* **2013**, *52*, 4024.

[111] M. Abel, S. Clair, O. Ourdjini, M. Mossoyan, L. Porte, *J. Am. Chem. Soc.* **2011**, *133*, 1203.

[112] O. Díaz Arado et al., *Chem. Commun.* **2015**, *4*, 1166.

[113] H.-Y. Y. Gao et al., *J. Am. Chem. Soc.* **2014**, *136*, 9658.

[114] L. A. Girifalco, *J. Phys. Chem.* **1992**, *96*, 858.

[115] F. van Zeggeren, G. C. Benson, *J. Chem. Phys.* **1957**, *26*, 1077.

[116] J. J. Gilman, *J. Appl. Phys.* **1960**, *31*, 2208.

[117] N. H. N. de Leeuw, S. C. S. Parker, *J. Phys. Chem. B* **1998**, *102*, 2914.

[118] L. Vitos, a.V. Ruban, H. Skriver, J. Kollár, *Surf. Sci.* **1998**, *411*, 186.

[119] W. Tyson, W. Miller, *Surf. Sci.* **1977**, *62*, 267.

[120] J. Fu, W. Chu, R. Dixson, T. Vorburger, *Scanning* **2008**, *30*, 41.

[121] D. Nečas, P. Klapetek, *Cent. Eur. J. Phys.* **2011**, *10*, 181.

[122] F. Loske, P. Rahe, A. Kühnle, *Nanotechnology* **2009**, *20*, 264010.

[123] P. Rahe, M. Nimmrich, A. Kühnle, *Small* **2012**, *8*, 2969.

[124] C. M. Hauke, PhD Thesis, Johannes Gutenberg-Universität Mainz, **2013**.

[125] J. Wuesten, C. Ziegler, T. Ertl, *Phys. Rev. B* **2006**, *74*, 1.

[126] B. a. Jones et al., *Angew. Chem. Int. Ed.* **2004**, *43*, 6363.

[127] C. W. Tang, *Appl. Phys. Lett.* **1986**, *48*, 183.

[128] Z. Chen, M. G. Debije, T. Debaerdemaeker, P. Osswald, F. Würthner, *ChemPhysChem* **2004**, *5*, 137.

[129] T. Kunstmann et al., *Phys. Rev. B* **2005**, *71*, 121403.

[130] T. Wagner, a Bannani, C Bobisch, H Karacuban, R Möller, *J. Phys. Condens. Matter* **2007**, *19*, 056009.

[131] J. Ikonomov, O. Bauer, M. Sokolowski, *Surf. Sci.* **2008**, *602*, 2061.

[132] M. Fendrich, T. Kunstmann, *Appl. Phys. Lett.* **2007**, *91*, 023101.

[133] S. A. Burke et al., *Phys. Rev. Lett.* **2008**, *100*, 7.

[134] E. Le Moal, M. Müller, O. Bauer, M. Sokolowski, *Phys. Rev. B* **2010**, *82*, 1.

[135] M. Müller, J. Ikonomov, M. Sokolowski, *Surf. Sci.* **2011**, *605*, 1090.

[136] A. E. Goresy, G Donnay, *Science* **1968**, *161*, 363.

[137] J. Lewis, B. Redfern, F. Cowlard, *Solid. State. Electron.* **1963**, *6*, 251.

[138] D Boyd, *J. Mol. Graph. Model.* **2001**, *19*, 181.

[139] H. Kroto, J. Heath, S. O'Brien, R. Curl, R. Smalley, *Nature* **1985**, *318*, 162.

[140] H. Schuster, W. Krätschmer, *Von Fuller bis zu Fullerenen*, (Ed.: H. Schuster), Vieweg & Sohn, Braunschweig/Wiesbaden, First Edit, **1996**, pp. 53–80.

[141] W. H. Powell et al., *Pure Appl. Chem.* **2002**, *74*, 629.

[142] A. Hirsch, *Fullerenes and Related Structures*, Springer, Berlin, Heidelberg, **1999**.

[143] G. Stollhoff, H. Scherrer, *Mater. Sci. Forum* **1995**, *191*, 81.

[144] S. A. Burke, J. Mativetsky, S. Fostner, P. Grütter, *Phys. Rev. B* **2007**, *76*, 1.

[145] P. Heiney et al., *Phys. Rev. Lett.* **1991**, *66*, 2911.

[146] A. M. Rao et al., *Science (80-.).* **1993**, *259*, 955.

[147] M. Nunez-Regueiro, L. Marques, J. Hodeau, O. Béthoux, M. Perroux, *Phys. Rev. Lett.* **1995**, *74*, 278.

[148] S Park et al., *J. Appl. Phys.* **1998**, *84*, 1340.

[149] J. Onoe et al., *Mol. Cryst. Liq. Cryst.* **2000**, *340*, 689.

[150] R. Lindner et al., *Angew. Chem. Int. Ed.* **2014**, *53*, 7952.

[151] M. Nimmrich et al., *Phys. Rev. B* **2012**, *85*, 035420.

[152] D. Löffler, P. Weis, S. Malik, A. Böttcher, M. Kappes, *Phys. Rev. B* **2008**, *77*, 155405.

[153] H. Yoshida, *J. Phys. Chem. C* **2014**, *118*, 24377.

[154] D. W. Rankin, *CRC handbook of chemistry and physics*, *Vol. 15*, (Ed.: D. R. Lide), CRC Press/Taylor and Francis, Boca Raton, FL, 89th ed., **2009**.

[155] W. Krätschmer, L. D. Lamb, K. Fostiropoulos, D. R. Huffman, *Nature* **1990**, *347*, 354.

[156] H.-B. Li et al., *Chem. Sci.* **2014**, *5*, 3493.

[157] M. Mattesini et al., Electronic structure and optical properties of solid C60, **2009**.

[158] G. Wang, K. Komatsu, Y. Murata, M Shiro, *Nature* **1997**, *387*, 583.

List of Figures

List of Tables

List of acronyms

AFM	atomic force microscope
A-FB	amplitude feedback loop
AM	amplitude-modulation
CPD	contact potential difference
FM	frequency-modulation
NC-AFM	non-contact atomic force microscope
HOPG	highly oriented pyrolytic graphite
KPFM	Kelvin-probe force microscopy
LEED	low-energy electron diffraction
LUMO	lowest unoccupied molecular orbital
ML	monolayer
NHC	N-heterocyclic carbene
PLL	phase-locked loop
PSD	position sensitive diode
PTCDA	3,4,9,10-perylenetetracarboxylic dianhydride
QCM	quartz-controlled micro-balance
SEM	scanning electron microscopy

SPM	scanning probe microscopy
STM	scanning tunnelling microscope
TCPTCDA	1,6,7,12-tetrachloro-3,4,9,10-perylenetetracarboxylic dianhydride
TPD	thermal programmed desorption
UHV	ultra-high vacuum
UPS	ultraviolet photo-electron spectroscopy
vdW	van-der-Waals

Publications & Contributions

Publications I have (co)-authored

- **Substrate Templating Guides the Photoinduced Reaction of C_{60} on Calcite.**
  R. Lindner, P. Rahe, M. Kittelmann, A. Gourdon, R. Bechstein, A. Kühnle
  Angew. Chem. Int. Ed. **53**, 7952 (2014)

- **Identifying the absolute orientation of a low-symmetry surface in real space**
  M. Kittelmann, M. Nimmrich, R. Lindner, A. Gourdon, A. Kühnle
  ACS Nano **7**, 5614 (2013)

- **From dewetting to wetting molecular layers: C_{60} on $CaCO_3(10\bar{1}4)$ as a case study.**
  P. Rahe, R. Lindner, M. Kittelmann, M. Nimmrich, A. Kühnle
  PCCP **14**, 6544 (2012)

- **Enhancing the molecule-substrate interaction by electron transfer through alkali metal doping**
  R. Lindner, D. Lautner, A. Kühnle
  Appl. Phys. Lett., *submitted 13.02.2015*

- **Review on On-Surface Synthesis**
  R. Lindner, A. Kühnle
  Chem. Phys. Chem, *submitted 26.02.2015*

- **Quantitative Analysis of the Substrate-Guided Polymerization of C_{60} on $CaCO_3$**
  R. Lindner, M. Stieffenhofer, A. Kühnle
  in preparation

- **Controlling Molecular Self-Assembly by Increasing Electrostatic Interactions**
  R. Lindner, J. Heidke, A. Kühnle
  in preparation

Talks

(presenting author underlined)

- **Lichtinduzierte Knüpfung von kovalenten Bindungen auf Isolatoren**
  R. Lindner, M. Kittelmann, P. Rahe, M. Nimmrich, C. M. Hauke, A. Kühnle
  (DPG Spring Meeting 2012, Berlin, Germany)

- **On-surface covalent linking on an insulating substrate**
  M. Kittelmann, R. Lindner, P. Rahe, M. Nimmrich, C. M. Hauke, A. Gourdon, A. Kühnle
  (DPG Spring Meeting 2012, Berlin, Germany)

- **Light induced covalent coupling of C_{60} on an insulator**
  R. Lindner,M. Kittelmann, P. Rahe, C. M. Hauke, A. Kühnle
  (Gordon Research Conference "Chemical Reactions on Surfaces", Les Diablerets, Switzerland)

- **Surface-guided photoreaction on an insulating substrate**
  R. lindner, M. Stieffenhofer, A. Gourdon, R. Bechstein, A. Kühnle
  (International Symposium on Surface Science 2014, Matsue, Japan)

Poster Presentations

(presenting author underlined)

- **Photopolymerization of C on insulating substrates**
  Robert Lindner, M. Kittelmann, P. Rahe , C. M. Hauke, M. Nimmrich, R. Bechstein, A. Kühnle
  (123rd BASF Summer Course 2012, Ludwigshafen, Germany)

- **Photopolymerization of C_{60} on insulating substrates**
  Robert Lindner, M. Kittelmann, P. Rahe , C. M. Hauke, M. Nimmrich, R. Bechstein, A. Kühnle
  (KIT NC-AFM Workshop 2013, Karlsruhe, Germany)

Acknowledgement

An dieser Stelle möchte ich allen Menschen danken, die dazu beigetragen haben, dass diese Arbeit in der vorliegenden Form existieren kann:

Mein ganz besonderer Dank gilt

- ... [redacted] für die hervorragende Betreuung während der letzten drei Jahre, eine immerfort offene Tür für Fragen und Diskussionen, und eine beispiellose Geschwindigkeit bei der Korrekturlesung von Manuskripten,
- ... [redacted] für die Zweitbetreuung der Doktorarbeit, sowie konstruktive Diskussionen im Rahmen der Thesis Committee Meetings,
- ... [redacted] für den Prüfungsvorsitz,
- ... [redacted] für die sehr gute Betreuung im Rahmen des Thesis Committee.
- ... [redacted] für die erhaltene Förderung als Stipendiat.

Desweiteren möchte ich hervorheben

- ... [redacted] für positiv prägende wissenschaftliche Diskussionen und die Hingabe zur deutschen Sprache.
- ... [redacted] für die exzellente Vorarbeit in meinem Promotionsthema, sowie die Hilfestellung in allen Belangen der UHV-Technik,
- ... [redacted] für eine fortwährende Diskussionsbereitschaft, die auch über die Wissenschaft hinaus gingen,
- ... [redacted] dessen erzieherische Maßnahmen die Integration von "Kevin" in die Arbeitsgruppe grundlegend verbessert haben,
- ... [redacted] für die ausführlichen Erklärungen zur KPFM-Technik, unabhängig von der Trivialität der Fragen,

· · · [redacted] für die sehr gute Arbeit während der von mir betreuten Bachelorarbeit,

und selbstverständlich

· · · [redacted] für die kontinuierliche Unterstützung und Hilfsbereitschaft in einer offenen Atmosphäre.

Abseits der Wissenschaft gilt mit Sicherheit der größte Dank

· · · [redacted] für die Unterstützung in allen Lebenslagen,

· · · [redacted] für die amüsanten Zeiten jenseits des UHV-Tellerrandes.

A

Further spectra on photopolymerized C_{60} films

A.1 UV-Vis spectra

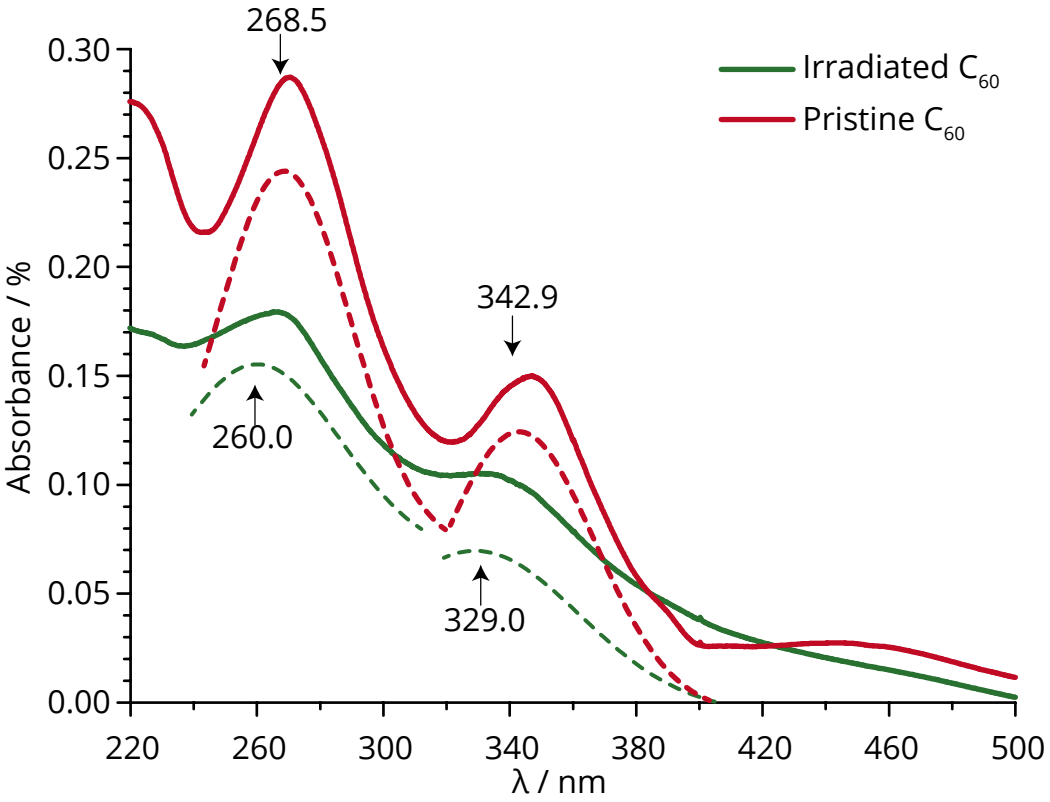

Fig. A.1.: UV-Vis spectra of pristine and photopolymerized C_{60} thin films on $CaCO_3$.

In order to verify the polymerization, UV-VIS-spectroscopy was performed on thin films of C_{60} pristine and irradiated samples. Due to the little signal of submonolayers of C_{60}, a higher film thickness was chosen.

All sample preparation was done under ultra-high vacuum conditions. Thin films of C_{60} on calcite were prepared by sublimation of C_{60} at a temperature of 378 °C for 43 minutes. This resulted in a calculated film thickness of 100 monolayers. The irradiation was carried out according to the experimental section.

UV-VIS-spectra were recorded with a JASCO V-530 Spectrophotometer.

The observed peaks for the pristine sample (red curve in Fig. A.1) are in excellent agreement with previously reported spectra[155] and theoretical calculations.[157]

Upon irradiation we observe a shift of the first peak from about 343 nm to 329 nm, which corroborates the successful photopolymerization of C_{60}.[158]

A.2 MALDI-TOF spectra

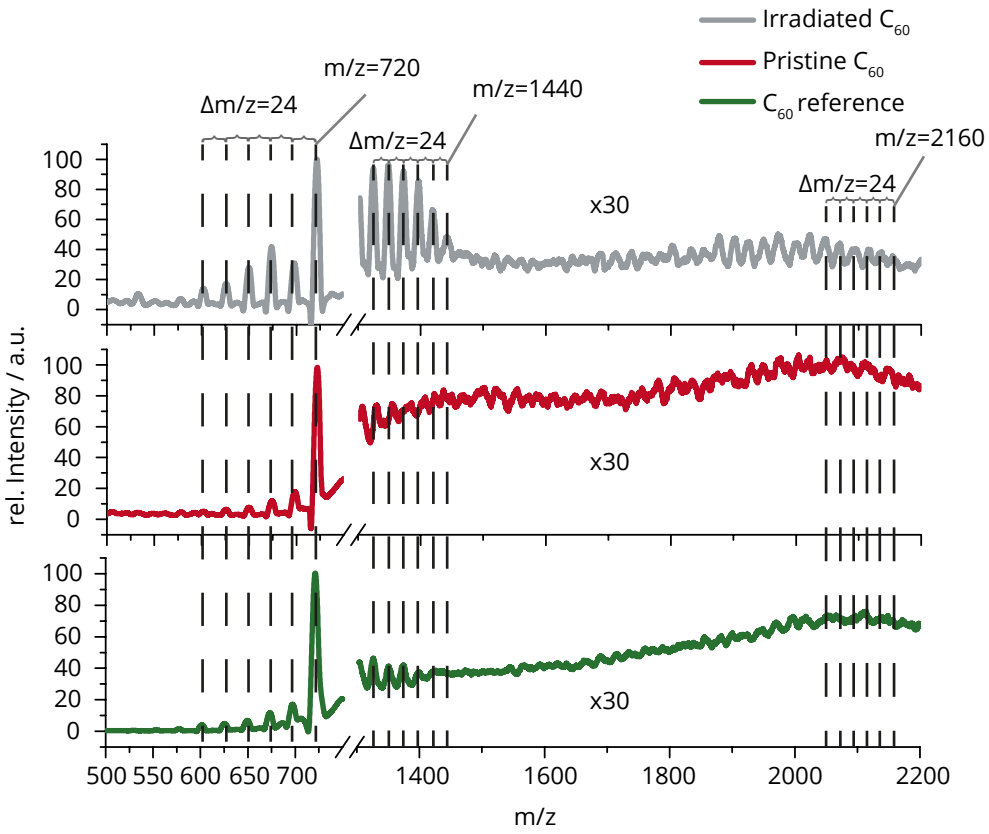

Fig. A.2.: MALDI-TOF spectra of pristine and photopolymerized C_{60} thin films.

Further analysis was carried out by laser-desorption-ionization time-of-flight mass spectrometry. The spectra were recorded with a Kratos mass spectrometer, utilizing a 366 nm laser with a power of 405 µJ/cm^2 for the desorption. The C_{60} thin films were dissolved from the crystal by thoroughly rinsing the coated surface of the crystal with 2×100 µL 1,2-Dichlorobenzene (anhydrous, >99%, Sigma Aldrich). Additionally a pure, pristine C 60 samples was measured for reference purposes.

The spectra exhibit a strong peak at 720 g/mol, corresponding to a single C_{60} molecule. Additionally a series of peaks with an interpeak distance of Δm/z=24 is visible, indicating the loss of C_{2n}-fragments.[158] The expected peak of the C_{60} dimer at m/z=1440 is clearly visible for the irradiated sample. For the pristine sample and the reference, a small amount ofC_{120} can be found, especially via the series of peaks, corresponding to the loss of C_{2n}. Since the spectra are normalized to the intensity of the C_{60} monomer peak at m/z = 720, it can be seen very clearly that the amount of C_{120} is substantially higher in the irradiated sample. Additionally a

weak signal at m/z = 2160, along with another series of peaks, can be observed for the irradiated sample, indicating a C_{60} trimer.

B

MatLab Code for $C_{60}C_{60}$ Distance Histograms

```
clear all

%read directory
dir = '.\images';
outputdir = '.\output\';

files = rdir('.\images*\*.txt');

        %pwd;
        %mydir = pwd;
        %dir = ['mydir'\images];
        %outputdir = ['mydir'\output];

        %files = rdir('mydir'\images*\*.txt);

imagewidth = 26.1;

Dtotal = [];
totalarea=0;
nummol=0;

for cell = 1:length(files)

% read image
im = load(files(cell).name);

% convert to gray level and normalize
img = mean(im,4);
img = mat2gray(img);


% search for image borders and nirvana from drift correction
corners = [img(1,1) img(1,end) img(end,1) img(end,end)];
borders = [img(1,:) img(end,:) img(:,1)' img(:,end)'];
val=corners(1);
count = sum(val==borders);
for i=2:4
if count < sum(corners(i)==borders)
val = corners(i);
count = sum(val==borders);
end
```

```
42 end
43 pos = img == val;
44 pos2 = medfilt2(pos, [3 3]);
45
46 %determine surface of image
47 area=sum(pos==0);
48 area=sum(area,2);
49 area=area.*(17.4/500)^2;
50
51 totalarea=totalarea+area;
52 nummol=nummol+(area/(sqrt(3)/6));
53
54 % low pass
55     lp = fspecial('gaussian', 50, 2.5);
56     imlp = imfilter(img, lp, 'same');
57
58 % allocate memory
59 [H W] = size(imlp);
60 blobs = zeros(H, W);
61
62 % non-max suppression with window size 2S+1
63 S = 3;
64 for i=S+1:H-S
65   for j=S+1:W-S
66      if pos2(i,j) == 0
67       local = imlp(i-S:i+S, j-S:j+S);
68       center = imlp(i,j);
69       if ~(max(local - center) > 0)
70           if ~(center == 0)
71             blobs(i,j) = 1;
72           end
73       end
74      end
75   end
76 end
77
78 %manual selection of leftover peaks
79
80 fpic = figure();
81 img(blobs==1) = 2;
82 imagesc(img);
83 axis('square');
84 ylabel('y / px');
85 xlabel('x / px');
86 colormap gray;
87 colormapeditor
88
89 %colormap reigreen(256);
90
91 [peaksx,peaksy] = ginput;
92
```

```
93  peaksx = round(peaksx);
94  peaksy = round(peaksy);
95
96  for p=1:length(peaksx)
97     blobs(peaksx(p),peaksy(p))=1;
98  end
99
100 %find row and column values
101
102 [row,col] = find(blobs);
103 D = zeros(length(row)-1);
104
105 for a = 1:length(row)
106     d = sqrt((row - row(a)).^2 + (col - col(a)).^2);
107     d = d(d>0);
108
109     D(a,:) = d;
110 end
111
112 D2 = D(D>15);
113 D3 = D2(D2<25);
114
115 [f_pathstr, f_name, f_ext] = fileparts(files(cell).name);
116 smallhisto = [D3.*imagewidth./500];
117 filename_print = [outputdir f_name  '_output'];
118 save([filename_print '.dat'], 'smallhisto', '-ascii');
119 title(['Found peaks in ' f_name],'Interpreter', 'none');
120 print(fpic, [filename_print '.jpg'], '-djpeg');
121 close(fpic);
122
123 fh = figure();
124 [n,xn] = hist(D3(:), 30);
125 xn = xn.*(imagewidth/500);
126 bar(xn,n);
127 ylabel('Counts');
128 xlabel('C_{60}-C_{60}-distance / nm');
129 title(['Histogram from : ' f_name],'Interpreter', 'none');
130 print(fh, [filename_print 'hist.jpg'], '-djpeg');
131 close(fh);
132
133 Dtotal = [Dtotal; D3];
134
135 %display
136
137 % fpic = figure();
138 % img(blobs==1) = 2;
139 % imagesc(img);
140 % axis('square');
141 % ylabel('y / px');
142 % xlabel('x / px');
143 % colormap gray;
```

```
144 % %colormap reigreen(256);
145 % title(['Found peaks in ' f_name],'Interpreter', 'none');
146 % print(fpic, [filename_print '.jpg'], '-djpeg');
147 % close(fpic);
148
149 end
150
151 fh_total = figure();[n,xn] = hist(Dtotal(:), 30);
152 xn = xn.*(imagewidth./500);
153 bar(xn,n);
154 ylabel('Counts');
155 xlabel('C_{60}-C_{60}-distance / nm');
156 title(['Hist total; number of images:' num2str(length(files)) ';Total
        area:' num2str(totalarea) 'nm^2 ;#molecules:' num2str(nummol)]);
157
158 histo = [Dtotal.*imagewidth./500];
159 filename_print_total = [outputdir 'total_output'];
160 save([filename_print_total '.dat'], 'histo', '-ascii');
161 print(fh_total, [filename_print_total '.jpg'], '-djpeg');
162 close(fh_total);
```

C MatLab Code Used for Drift Correction

C.1 Sample tilt correction

```
function [images,driftmatrix] = tilt_correction(images,driftmatrix)

% Automatic tilt correction for SPM images by coordinate transformation,
% based on the method by
%   J. Fu, et al., Scanning, Vol.30, p.41 (2008).
%


%read files
%images = dir(fullfile('D:', 'Matlab', 'zdrift correction', '*.txt'));

for file=1:length(images)

data = images(driftmatrix(file,1),1).values;

data=data*10^12; %prevent rounding errors

%initialize parameters
R=zeros(4,4);
coords=ones(250000,4);
rotcoords=ones(250000,4);
k=0;
R(4,4)=1;%initialize rotation matrix

[y x] = meshgrid(1:500,1:500);  % coordinates of the plane
A = [ones(numel(y),1) y(:) x(:)];      % prepare least-square fit
planecoeff = A\data(:);      % execute fit

z_axis=[-planecoeff(2,1);-planecoeff(3,1);1];%determine new z-axis

%determine new x-axis
p1= [0 0 planecoeff(1,1)]';
z=10000000000*planecoeff(2,1)+planecoeff(1,1);%high x-value due to matlab rounding error
p2= [10000000000 0 z]';

x_axis= p2-p1;
```

```
37
38
39 y_axis=cross(z_axis,x_axis);%determine new y-axis
40
41 %normalize new axes
42 x_norm=x_axis/norm(x_axis);
43 y_norm=y_axis/norm(y_axis);
44 z_norm=z_axis/norm(z_axis);
45
46 x_norm(4,1)=1;
47 y_norm(4,1)=1;
48 z_norm(4,1)=1;
49
50 %write values to rotation matrix
51 for i=1:3
52    R(i,1)=x_norm(i,1);
53    R(i,2)=y_norm(i,1);
54    R(i,3)=z_norm(i,1);
55 end
56
57 %reshape image to xyz-vector
58 for l=1:500
59     for m=1:500
60         k=k+1;
61         coords(k,1)=l;
62         coords(k,2)=m;
63         coords(k,3)=data(m,l);
64     end
65 end
66
67 %multiply every data point with rotation matrix
68 for p=1:250000
69     rotcoords(p,:)=coords(p,:)*R;
70 end
71
72 %recreate image
73 data=reshape(rotcoords(:,3),500,500);
74 %figure(1);imagesc(test);
75 %figure(2);imagesc(test2);
76 images(driftmatrix(file,1)).values=data;
77 [~, name, ~] = fileparts(images(driftmatrix(file,1)).name);
78
79 fprintf('Tilt correction of "%s", image %d of %d succesful.\n', name,
       file, length(images));
80 end
```

C.2 Z-Drift Correction

```
function [images,driftmatrix] = z_drift(images,driftmatrix)

% Automatic z-drift correction for SPM images,
% based on the method by
%   P. Rahe, et al., J. Vac. Sci. Technol. B., Vol.28, p.C4E31 (2010).

%set parameters

% parameters=cell(length(images)+1,4);
scantime = 522; %time in sec for one image
numpixel=500;%number of pixels in x and y-direction

disp('Calculating z-drift correction.');

%load individual files into data-matrix

for file=1:length(images)

    data = images(driftmatrix(file,1),1).values;

    %calculate mean height

    colsum = sum(data);
    rowsum = sum(colsum);%sum of all elements

    [cols,rows] = size(data);
    pixels = cols*rows;%number of pixels

    driftmatrix(file,6) = rowsum./pixels;
end

%calculate x-values aka scanning time

for p=1:length(images)
    driftmatrix(p,5) = (p-1)*522;
end

%linear fit of mean image height
fit = polyfit(driftmatrix(:,5),driftmatrix(:,6),1);
fitline=[2,2];

fprintf('The fitted linear equation is: y=%d *x+%d .\n', fit(1,1), fit
    (1,2));

%for x=1:2
%fitline(x,x)=fit(1,1)*x+fit(1,2);
%end

```

```
48 z_drift_fit=figure;
49 hold on
50
51 plot(driftmatrix(:,5),driftmatrix(:,6),'o');
52 plot(driftmatrix(:,5),polyval(fit,driftmatrix(:,5)));
53 title('Z-Drift');
54 xlabel('t/sec');
55 ylabel('Shift/nm');
56
57 hold off
58
59 print(z_drift_fit, 'z_drift_fit.png', '-dpng');
60
61
62 for file=1:length(images)
63
64     data = load(images(driftmatrix(file,1)).name);
65
66
67 %calculate values
68
69 %down
70
71 if driftmatrix(file,3)==0
72     %trace
73     if driftmatrix(file,4)==1
74         for i=1:numpixel
75             for j=1:numpixel
76                 data(i,j) = data(i,j)- fit(1,1)*(scantime/(2*numpixel*
                        numpixel))*(2*numpixel*(numpixel-i)+j)-fit(1,1)*
                        driftmatrix(file,5)-fit(1,2);
77             end
78         end
79     end
80     %retrace
81     if driftmatrix(file,4)==0
82         for i=1:numpixel
83             for j=1:numpixel
84                 data(i,j) = data(i,j)- fit(1,1)*(scantime/(2*numpixel*
                        numpixel))*(2*numpixel*(numpixel-i+1)-j+1)-fit
                        (1,1)*driftmatrix(file,5)-fit(1,2);
85             end
86         end
87     end
88 end
89
90 %up
91
92 if driftmatrix(file,3)==1
93     %trace
94     if driftmatrix(file,4)==1
```

```
95          for i=1:numpixel
96              for j=1:numpixel
97                  data(i,j) = data(i,j)- fit(1,1)*(scantime/(2*numpixel*
                        numpixel))*(2*numpixel*(numpixel+i-1)+j)-fit(1,1)*
                        driftmatrix(file,5)-fit(1,2);
98              end
99          end
100     end
101     %retrace
102     if driftmatrix(file,4)==0
103         for i=1:numpixel
104             for j=1:numpixel
105                 data(i,j) = data(i,j)- fit(1,1)*(scantime/(2*numpixel*
                        numpixel))*(2*numpixel*(numpixel+i)-j+1)-fit(1,1)*
                        driftmatrix(file,5)-fit(1,2);
106             end
107         end
108     end
109 end
110
111 %save corrected data into images-structure
112
113 images(driftmatrix(file,1)).values=data;
114 [~, name, ~] = fileparts(images(driftmatrix(file,1)).name);
115
116 % %create plot with all corrected images
117 % subplot(2,0.5*length(images),file);imagesc(data);
118 % set(gcf, 'Position', get(0,'Screensize')); % Maximize figure.
119 % axis square;
120 % %title('%s', image(file).name);
121
122 fprintf('Z-drift correction of "%s", image %d of %d succesful.\n',
        name, file, length(images));
123 end
124
125 %disp('All done!');
```

C.3 X/Y-Drift Correction

```
function [images,driftmatrix]=xy_drift(images,driftmatrix)

% Automatic xy-drift correction for SPM images by polynomial distortion,
% based on the method by
%   P. Rahe, et al., J. Vac. Sci. Technol. B., Vol.28, p.C4E31 (2010).
% written by Robert Lindner robert.lindner@uni-mainz.de

scantime=1;
T=522;%time for one pair of forward+backward images
% height=20;
% width=20;
prompt = 'What is the image height? (in nm)';%height of the image in nm
height = input(prompt);
prompt = 'What is the image width? (in nm)';%width of the image in nm
width = input(prompt);
pixelh=size(images(driftmatrix(1,1),1).values,1);%pixel height of image
pixelw=size(images(driftmatrix(1,1),1).values,2);
corrparam=zeros(4,3);%matrix for correction parameters

%create plot with two consecutive images

for file=1:2
    data = images(driftmatrix(file,1),1).values;
    subplot(1,2,file);imagesc(data);
    colormap(reigreen(256));
    set(gcf, 'Position', get(0,'Screensize')); % Maximize figure.
    axis square;
    str=sprintf('Image #%d : %s', file, images(driftmatrix(file,1),1).name);
    title(str, 'Interpreter', 'none');
end

[driftmatrix(1,7) driftmatrix(1,8)]=ginput(1);
hold on

 plot(driftmatrix(1,7),driftmatrix(1,8),'r+');
hold off

[driftmatrix(2,7) driftmatrix(2,8)]=ginput(1);

if length(images)>2

    for file=3:length(images)
        data = images(driftmatrix(file,1),1).values;
        subplot(1,2,2);imagesc(data);
```

```
45          colormap(reigreen(256));
46          set(gcf, 'Position', get(0,'Screensize')); % Maximize figure.
47          axis square;
48          str=sprintf('Image #%d : %s', file, images(driftmatrix(file,1)
                ,1).name);
49          title(str, 'Interpreter', 'none');
50          drawnow
51          [driftmatrix(file,7) driftmatrix(file,8)]=ginput(1);
52      end
53
54  end
55
56  %calculate feature position in meters
57  disp('Calculating drift velocities.');
58
59  for k=1:length(images)
60      driftmatrix(k,9)=driftmatrix(k,7)/pixelw*width;
61      driftmatrix(k,10)=driftmatrix(k,8)/pixelh*height;
62  end
63
64  %calculate time between scanning of feature in images
65
66  driftmatrix(1,11)=0;%first value is zero, obiously
67
68  for l=2:size(driftmatrix,1)
69
70      time=0;
71
72      if driftmatrix(1,3)==0
73          time=driftmatrix(1,8)*(pixelw*scantime+T);
74      else
75          time=(pixelh-driftmatrix(1,8))*(pixelw*scantime+T);
76      end
77
78      if (driftmatrix(l,2)-driftmatrix(1,2))>1
79          time=time+(driftmatrix(l,2)-driftmatrix(1,2)-1)*(2*size(data
                ,1)*(size(data,2)*scantime+T));
80      end
81
82      if (driftmatrix(l,2)-driftmatrix(1,2))>0
83          if driftmatrix(1,3)==0
84              time=time+(size(data,1)*(size(data,2)*scantime+T));
85          end
86          if driftmatrix(l,3)==1
87              time=time+(size(data,1)*(size(data,2)*scantime+T));
88          end
89      end
90
91      if driftmatrix(l,3)==0
92          time=time+((size(data,1)-driftmatrix(l,8))*(size(data,2)*
                scantime+T));
```

```
93      else
94          time=time+driftmatrix(l,8)*(size(data,2)*scantime+T);
95      end
96      time=time/1000;
97      driftmatrix(l,11)=time;
98  end
99
100 %linear fit of x-position
101 fitxpos = polyfit(driftmatrix(:,11),driftmatrix(:,9),1);
102 fitline=[2,2];
103
104 fprintf('X-Drift: y=%d *x+%d .\n', fitxpos(1,1), fitxpos(1,2));
105
106
107 %for x=1:2
108 %fitline(x,x)=fit(1,1)*x+fit(1,2);
109 %end
110
111 x_drift_fit=figure;
112 hold on
113
114 plot(driftmatrix(:,11),driftmatrix(:,9),'o');
115 plot(driftmatrix(:,11),polyval(fitxpos,driftmatrix(:,11)));
116 xlabel('t/sec');
117 ylabel('Shift/nm');
118 title('X-Drift');
119
120 hold off
121
122 print(x_drift_fit, 'x_drift_fit.png', '-dpng');
123
124 %linear fit of y-position
125 fitypos = polyfit(driftmatrix(:,11),driftmatrix(:,10),1);
126 fitline=[2,2];
127
128 fprintf('Y-Drift: y=%d *x+%d .\n', fitxpos(1,1), fitypos(1,2));
129
130 %for x=1:2
131 %fitline(x,x)=fit(1,1)*x+fit(1,2);
132 %end
133
134 y_drift_fit=figure;
135 hold on
136
137 plot(driftmatrix(:,11),driftmatrix(:,10),'o');
138 plot(driftmatrix(:,11),polyval(fitypos,driftmatrix(:,11)));
139 xlabel('t/sec');
140 ylabel('Shift/nm');
141 title('Y-Drift');
142
143 hold off
```

```
144
145 print(y_drift_fit, 'y_drift_fit.png', '-dpng');
146
147 %calculate correction parameters
148 negxpos=fitxpos(1,1);
149 negypos=fitypos(1,1);
150
151 corrparam(1,1)=negxpos*pixelh*(pixelw*scantime+T)/1000/height;
152 corrparam(1,2)=1;
153 corrparam(1,3)=negxpos*pixelh*(pixelw*scantime+T)/1000*height/(width*(
        height-negypos*pixelh*(pixelw*scantime+T)/1000));%vorzeichenfehler
154 corrparam(2,1)=negypos*pixelh*(pixelw*scantime+T)/1000/width;
155 corrparam(2,3)=1+negypos*height*(pixelw*scantime+T)/1000/(height-
        negypos*pixelh*(pixelw*scantime+T)/1000);
156 corrparam(3,2)=1;
157 corrparam(3,3)=negxpos*pixelh*(pixelw*scantime+T)/1000*height/(width*(
        height+negypos*pixelh*(pixelw*scantime+T)/1000));%vorzeichenfehler
158 corrparam(4,3)=1-negypos*pixelh*(pixelw*scantime+T)/1000/(height+
        negypos*height*(width*scantime+T)/1000);
159
160 %display correction parameters nicely
161 dispcorr=cell(5,4);
162 dispcorr{1,2}='F(11)';
163 dispcorr{1,3}='F(X1)';
164 dispcorr{1,4}='F(1Y)';
165
166 dispcorr{2,1}='Pxup';
167 dispcorr{3,1}='Pyup';
168 dispcorr{4,1}='Pxdown';
169 dispcorr{5,1}='Pydown';
170
171 for k=2:5
172     for l=2:4
173         dispcorr{k,l}=corrparam(k-1,l-1);
174     end
175 end
176 diary;
177 diary('correctionparameters.dat');
178 disp(dispcorr);
179 diary;
```

Colophon

This thesis was typeset with LaTeX 2$_\varepsilon$. It uses the *Clean Thesis* style developed by Ricardo Langner. The design of the *Clean Thesis* style is inspired by user guide documents from Apple Inc.

Download the *Clean Thesis* style at `http://cleanthesis.der-ric.de/`.

Declaration

Hiermit versichere ich, dass ich die vorliegende Arbeit selbst angefertigt habe und nur die genannten Quellen benutzt habe

Mainz, den 27. Februar 2015

Robert Lindner